Journal of Volcanology and Geothermal Research 323 (2016) 19–37

Contents lists available at ScienceDirect

Journal of Volcanology and Geothermal Research

journal homepage: www.elsevier.com/locate/jvolgeores

The temporal evolution of back-arc magmas from the Auca Mahuida shield volcano (Payenia Volcanic Province, Argentina)

Carlos Pallares [a,*], Xavier Quidelleur [a], Pierre-Yves Gillot [a], Jean-Michel Kluska [b], Paul Tchilinguirian [c,d], Philippe Sarda [a]

[a] GEOPS, Univ. Paris-Sud, CNRS, Université Paris-Saclay, Rue du Belvédère, Bât. 504, 91405 Orsay, France
[b] TOTAL SA, France
[c] CONICET, Argentina
[d] FCEyN, Universidad de Buenos Aires, Argentina

ARTICLE INFO

Article history:
Received 18 September 2015
Received in revised form 3 March 2016
Accepted 29 April 2016
Available online 10 May 2016

Keywords:
K–Ar ages
OIB-type magmas
Auca Mahuida volcano
Los Volcanes
Payenia Volcanic Province
Argentina

ABSTRACT

In order to better constrain the temporal volcanic activity of the back-arc context in Payenia Volcanic Province (PVP, Argentina), we present new K–Ar dating, petrographic data, major and trace elements from 23 samples collected on the Auca Mahuida shield volcano. Our new data, coupled with published data, show that this volcano was built from about 1.8 to 1.0 Ma during five volcanic phases, and that Auca Mahuida magmas were extracted from, at least, two slightly different OIB-type mantle sources with a low partial melting rate. The first one, containing more garnet, was located deeper in the mantle, while the second contains more spinel and was thus shallower. The high-MgO basalts (or primitive basalts) and the low-MgO basalts (or evolved basalts), produced from the deeper and shallower lherzolite mantle sources, respectively, are found within each volcanic phase, suggesting that both magmatic reservoirs were sampled during the 1 Myr lifetime of the Auca Mahuida volcano. However, a slight increase of the proportion of low-MgO basalts, as well as of magmas sampled from the shallowest source, can be observed through time. Similar overall petrological characteristics found in the Pleistocene–Holocene basaltic rocks from Los Volcanes and Auca Mahuida volcano suggest that they originated from the same magmatic source. Consequently, it can be proposed that the thermal asthenospheric anomaly is probably still present beneath the PVP. Finally, our data further support the hypothesis that the injection of hot asthenosphere with an OIB mantle source signature, which was triggered by the steepening of the Nazca subducting plate, induced the production of a large volume of lavas within the PVP since 2 Ma.

© 2016 Elsevier B.V. All rights reserved.

1. Introduction

A unique back-arc Plio-Quaternary intraplate volcanic province lies to the west of the Southern Volcanic Zone (SVZ) that was built by the subduction of the Nazca oceanic lithosphere underneath the South American plate (Fig. 1). This province, referred to here as the Payenia Volcanic Province (PVP), is made of several composite volcanoes and wide volcanic fields accounting for a large arc-parallel area developed between 35° and 38°S. The origin of back-arc magmatism has been related to changes affecting the dip of the subducting slab (e.g., Ramos et al., 2014; Kay et al., 2006a), which induced a complex interaction between asthenosphere and lithosphere into the mantle wedge beneath this zone.

The geochemical affinities found in the Plio-Quaternary back-arc basalts from the PVP vary significantly, including intraplate (OIB-type) or arc-related signatures (Kay et al., 2006a, 2013; Søager et al., 2013; Søager and Holm, 2013; Hernando et al., 2014a). The description of the spatial and temporal evolution of this exceptional geological province is therefore of major relevance. It was recently analyzed by several authors: the relationship between volcanism and deformational events, the geometry of the subducting slab, the nature of associated magmatism and its sources (e.g., Ramos et al., 2014; Hernando et al., 2012, 2014a, 2014b; Kay et al., 2006a, 2013; Søager et al., 2013, 2015a, 2015b; Søager and Holm, 2013; Dyhr et al., 2013a, 2013b; Gudnason et al., 2012; Ramos and Folguera, 2011; Llambías et al., 2010; and references therein).

Among the large Plio-Quaternary volcanic complexes present in the PVP (Fig. 1), the Auca Mahuida is the only shield-type volcano in the PVP. It appears as a key edifice due to its position, volume, and magmatic type, and also because it lies in the southernmost position within the so-called Central Depression, a part of the Cortaderas lineament, which marks the southern end of the Plio-Quaternary back-arc volcanism (Søager et al., 2013). The Auca Mahuida volcano erupted an important volume of lava and displays an intraplate OIB-type signature (Kay et al., 2004, 2006a, 2013; Bertotto et al., 2009; Søager et al., 2013; Søager and Holm, 2013; Hernando et al., 2014a).

* Corresponding author.
E-mail address: carlos.pallares@u-psud.fr (C. Pallares).

http://dx.doi.org/10.1016/j.jvolgeores.2016.04.043
0377-0273/© 2016 Elsevier B.V. All rights reserved.

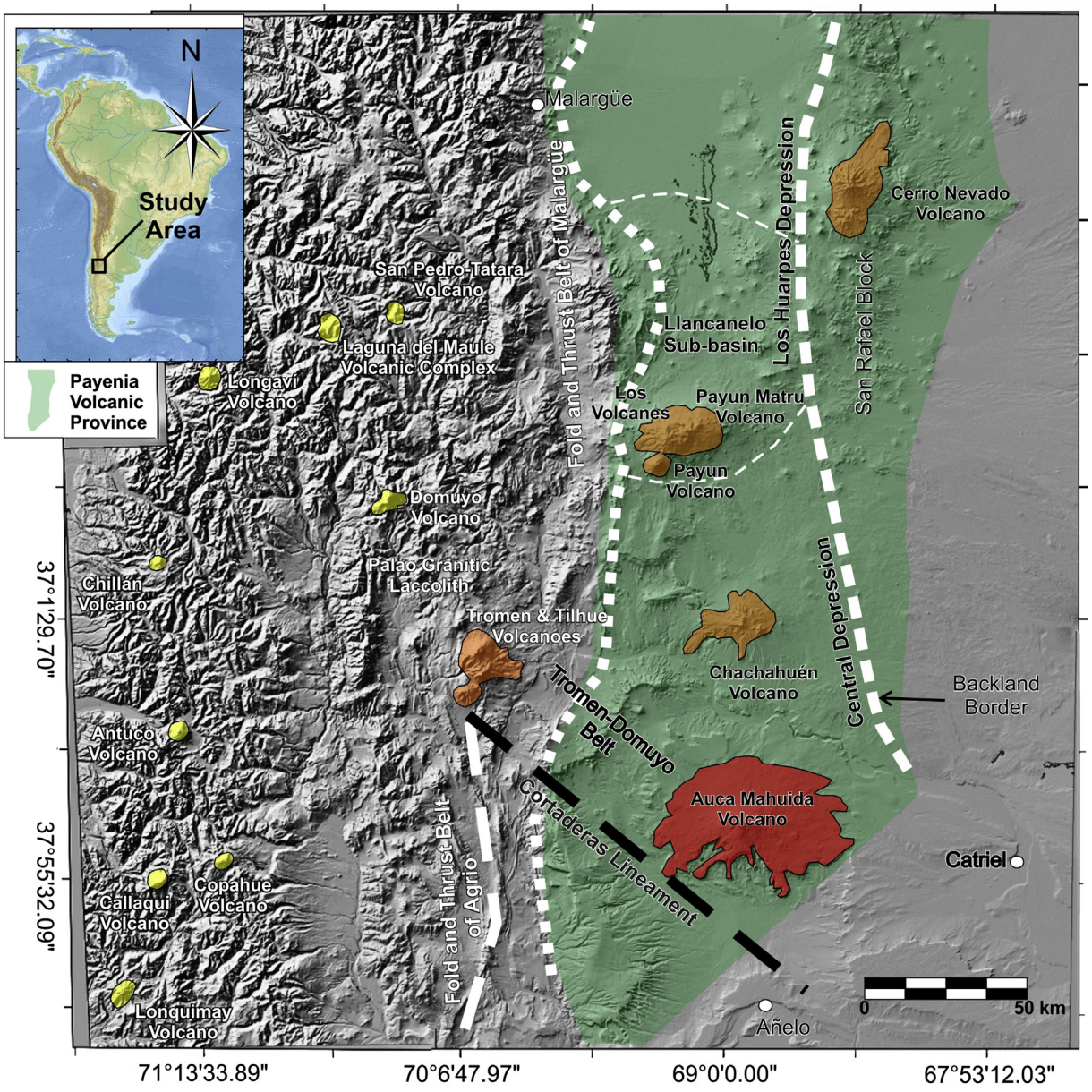

Fig. 1. Shaded view of the digital elevation model (DEM) at a resolution of 1:90,000 (Shuttle Radar Topography Mission: SRTM data) of the studied area. Coordinates are in UTM. Insert: location of the studied area within South-America. Modified from Ramos and Kay (2006) and Llambías et al. (2010). Green field: Payenia Volcanic Province; red field: Auca Mahuida shield volcano; orange fields: other volcanoes; large dotted line: Fold and thrust belt of Agrio and Cortaderas Lineament; medium dotted line: Backland border; small dotted line: Fold and thrust belt of Malargüe. (For interpretation of the references to color in this figure legend, the reader is referred to the online version of this chapter.)

In this paper, we present new K–Ar ages, major and trace element data from the Auca Mahuida shield volcano, in order to better describe its magmatic evolution, and to investigate its relationship with other young back-arc volcanoes in the PVP.

2. Geological setting

2.1. Back-arc magmatism of the PVP

The Miocene–Quaternary geological history of PVP and surrounding areas (Fig. 1) was marked by a major change of the subduction geometry, from a shallowed slab regime at the end of the Miocene to a normal ~30° dip subduction since about 4 Ma (Kay et al., 2004, 2006a, 2006b; Ramos and Kay, 2006). Between 8 and 3.5 Ma (Kay et al., 2006a; Litvak et al., 2015), the volcanic activity in the foreland had a mainly subduction-related affinity, as shown by the Chachaúén lavas (Kay et al., 2006b), or, the eastern mesosilicic volcanic centers from San Rafael Block (Litvak et al., 2015). A compressional tectonic regime, associated with the Payenia shallow subduction (Ramos et al., 2014 and references therein), redeformed in the late Miocene (Folguera et al., 2015a; Fennell et al., 2015) the Malargüe fold and thrust belt (Fig. 1) initially generated in the Cretaceous–Eocene times. Overall, the Payenia shallow subduction triggered an important compression episode in the whole Andean foothills (Ramos and Folguera, 2005; Ramos and Kay, 2006). Afterwards, the steepening of the Nazca oceanic subducting plate caused an extensional tectonic regime (Kay et al., 2006a; Ramos and Kay, 2006; Gudnason et al., 2012) thinning the crust to less than 42 km in the axial part of the PVP (Ramos et al., 2014). This event produced the development of the Central Depression tectonic structure (Ramos and Folguera, 2011; Fig. 1), also referred to as the Los Huarpes Depression in its northern part (Llambías et al., 2010). This extensional setting beneath the PVP also favored the increase of volcanic activity since 2 Ma,

with the formation of about 800 monogenetic basaltic cones and a few polygenetic volcanic complexes (Bermúdez et al., 1993; Folguera et al., 2009; Llambías et al., 2010).

Overall, magmatic rocks from PVP contain to some extent arc-magmatism characteristics, where magma is generated by hydrous fluxing and melting of the mantle wedge during the subduction of the Nazca plate. However, some back-arc rocks do not display subduction-related affinity and have been linked to the injection of hot asthenosphere producing intraplate rocks (also termed: OIB-type rocks; Kay et al., 2004, 2006a, 2013; Bertotto et al., 2009; Søager et al., 2013, 2015a, 2015b; Søager and Holm, 2013; Hernando et al., 2014a) during steepening of the subducting slab. Although the origin and evolution of these back-arc rocks is complex, the authors generally agree with a magmatic genesis produced in the mantle asthenosphere, and a probable northward migration based on pronounced geochemical differences and geochronological data between the southern and northern PVP basalts from the last 2 Ma (Gudnason et al., 2012; Søager et al., 2013; Søager and Holm, 2013). Southern back-arc basaltic rocks are thought as sourced from an EM1-like mantle where eclogite and peridotite melts interacted at different pressures, with a small or null contribution of subduction-related components (Søager et al., 2013; Søager and Holm, 2013), or as resulting from mixing of an EM1 ocean island basalt type, pyroxene-rich source and a peridotitic source with more radiogenic Pb that was metasomatized by subduction-zone fluids and/or melts (Søager et al., 2015b). Or else, these basaltic lavas are sourced from an EM1-like garnet-bearing mantle at 4–7% melting, above a steepening subduction zone, and finally mixed with continental lithosphere after storage near the base of a 65–70 km-thick lithosphere (Kay et al., 2013). The last interpretation from Kay et al. (2006b, 2013) is based on the high Sr and Ba contents of the Auca Mahuida lavas, which are interpreted as reflecting the residues of arc components that were introduced into the continental lithosphere during the shallow subduction stage. This lithospheric component was proposed to enter the Auca Mahuida magmas as they stall at the base of lithosphere and ascend. In contrast, the northern back-arc basaltic rocks were sourced from a similar to normal MORB mantle, which was affected by addition of fluids and melts from the subducting slab (Søager et al., 2013, 2015a).

2.2. The Auca Mahuida shield volcano

The Auca Mahuida shield volcano, was emplaced in the Malargüe fold and thrust belt that deforms the Mesozoic Neuquén sedimentary Basin. It is the southernmost volcanic edifice from the PVP (Llambías et al., 2010). It displays a semicircular structure with a diameter of about 50 km and an altitude of 2250 m above sea level. It has an overall E–W elongated morphology with a high density of parasitic cones following the same main orientation (Ventura et al., 2012). A central cone of 15 × 11 km with 30° slope and a 2 km wide summit caldera is present (Risco Alto Auca Mahuida). Examination of the Landsat 7 satellite images reveals that several other eruption centers existed, such as Cerro La Faja or Cerro de Los Ingenieros, and that lavas could have also been erupted from lateral fractures, obliterated by younger lavas (Fig. 2). In addition, we note the occurrence of short and thick viscous lava flows close to the summit caldera, as also observed on the Payun Matrú volcano (e.g., Germa et al., 2010). The area has been widely investigated for oil and gas exploration but published studies remain scarce.

The Auca Mahuida shield volcano was constructed during the Quaternary (Holmberg, 1964; Rossello et al., 2002; Kay et al., 2006a, 2013; Ramos and Folguera, 2011), but its temporal evolution remains poorly constrained because only a few reliable radiometric ages have been published. The lavas from Auca Mahuida volcano, which belong to the alkaline series, present geochemical similarities with those from Payún Matrú and Llancanelo volcanic fields, such as intraplate features (Bermúdez et al., 1993; Kay et al., 2004, 2006a, 2013; Bertotto et al., 2009; Søager et al., 2013; Søager and Holm, 2013; Hernando et al., 2014a).

3. Material and methods

3.1. Sampling

We have collected 23 samples in the central and southern part of the Auca Mahuida shield volcano (Fig. 2). All of them (except AM82 and AM40) were analyzed for major and trace elements, and 11 were dated using K–Ar. Our sampling was aimed to complete the previously available data set from Auca Mahuida volcano (Ardolino et al., 1995; Rossello et al., 2002; Kay et al., 2004, 2006a, 2013; Gudnason et al., 2012; Jacques et al., 2013), and our samples fall in younger and/or older mapped categories (Fig. 2). Based on the geological map (Ardolino et al., 1995), our samples are mainly located in a zone delimited by the Rincón del Palo Blanco Canyon, Cerro La Faja, the main caldera, and Cerro de Los Ingenieros (Figs. 2 and 3). In addition, some samples are located on the southeast side of the main shield (AM28 and AM52) and others lie to the north of main caldera (AM71 and AM82). Using the different units from the stratigraphic sequence (Ardolino et al., 1995; Fig. 3) our samples belong to Pampa de Las Yeguas Basalt (AM37), La Faja Basalt (AM52, AM26, AM71), Rincon del Infiernillo Basalt (88AI, 88AJ, 88AH, 88AK, 88AG, AM33), Pampa del Leon Basalt (AM79, AM82, AM28, AM40), Auca Mahuida Trachyandesite (AM66, AM50, AM7, AM8), Puesto Retamal Trachyandesite (AM70, AM45, AM31, 88AE) and Aguada Lastra Volcanics (88AF). Most of analyzed samples come from lava flows, except some which have been taken from pyroclastic deposits (AM31) or lava domes (AM8, 88AE).

3.2. Major and trace element composition

The geochemical data have been analyzed by the Service d'Analyse des Roches et Minéraux (SARM) at Centre de Recherches Pétrographiques et Géochimiques de Nancy, France (CRPG). The major elements data were obtained by Inductively Coupled Plasma-Atomic Emission Spectrometry (ICP-AES: Thermo Electron IRIS Advantage) and the trace elements by Inductively Coupled Plasma-Mass Spectrometry (Thermo Elemental X7). Overall, our analyzed samples lack secondary minerals, except carbonate and zeolite minerals that fill some vesicles in rare cases, but they have been removed during sample preparation. The samples were then finely powdered in an agate grinder; 200 mg of rock was melted with $LiBO_2$ in Pt–Au crucible, and then dissolved with HNO_3. International standards were used for calibration tests (AN-G, BR, UB-N, DR-N, GH), which underwent the same processing (Carignan et al., 2001; Govindaraju and Mevelle, 1987; Govindaraju and Potts, 1994). Analytical uncertainties for each element can be found on the SARM-CRPG website at: http://helium.crpg.cnrsnancy.fr/SARM/index.html.

3.3. K–Ar dating

In order to provide strong geochronological constraints, we have dated 11 samples from the Auca Mahuida using the K–Ar Cassignol–Gillot technique (Cassignol and Gillot, 1982; Gillot and Cornette, 1986). This technique was successfully applied to volcanic rocks from the Cerro Nevado (1.88 ± 0.03–0.94 ± 0.01 Ma; Quidelleur et al., 2009) and Payun Matrù (285 ± 5–<7 ± 1 ka; Germa et al., 2010). It allows accurate dating of both ancient and young lavas, even of samples with low radiogenic argon content. In order to avoid K loss due to weathering, as well as excess argon carried by mafic minerals and low K content plagioclases, analyses were performed on groundmass, in a narrow density range phase. Only sample AM8 was dated using alkali feldspars. Selected rocks were processed according to phenocrysts size, with crushing and sieving at typically 125–250 μm or 100–200 μm. Grains were

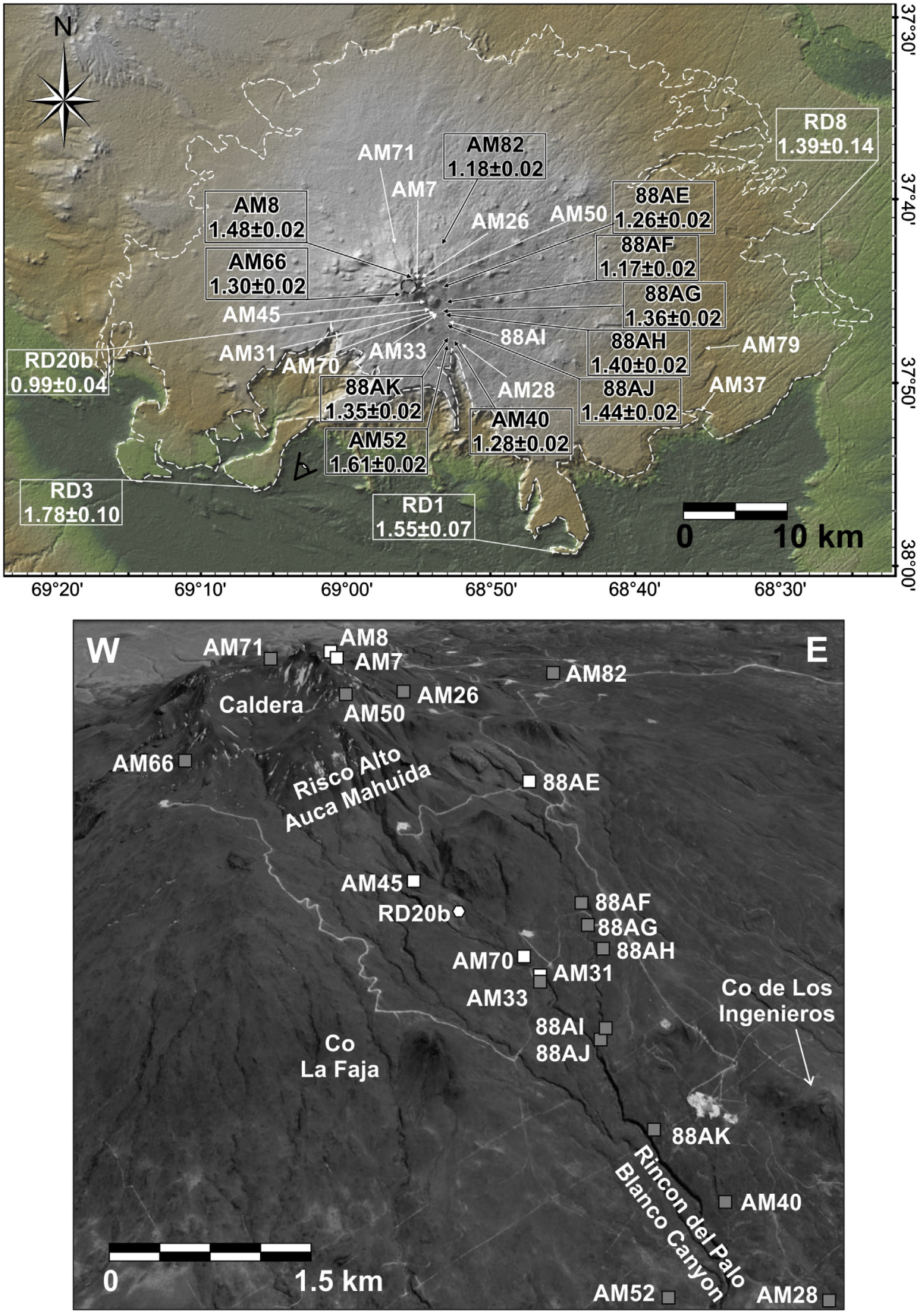

Fig. 2. Vertical and oblique views of the Auca Mahuida volcano and studied area, respectively, obtained using GMRT (a) and Google Earth (a) images. Samples from this study (labels 88XX and AMXX) are shown with a grey (basaltic rocks) or white (andesitic rocks) square symbol. Those from Kay et al. (2004, 2006a, label RDX), and associated ages in Ma, are shown with gray and white hexagons.

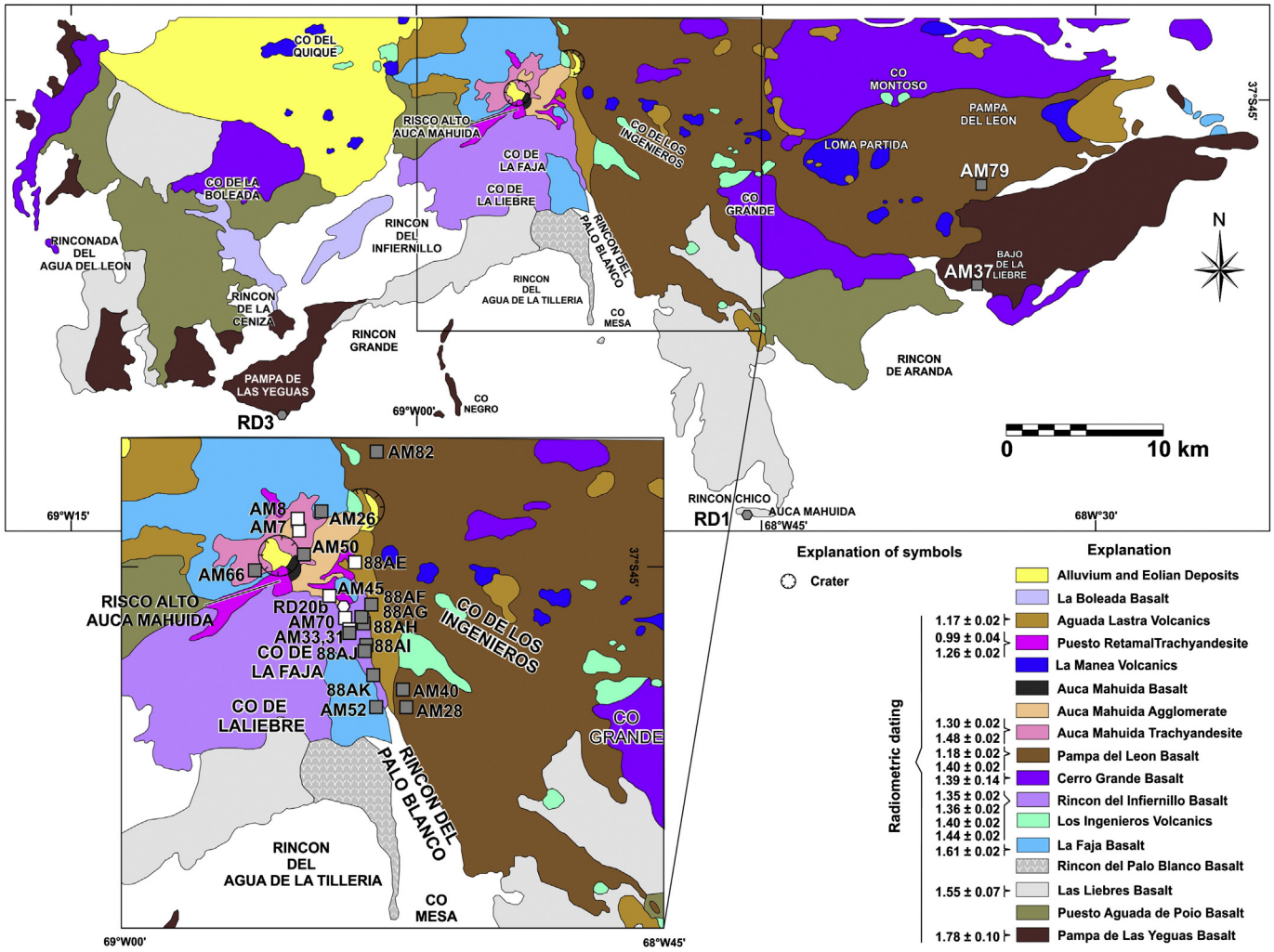

Fig. 3. The main volcanic formations within the studied area are from the Geological Map of Añelo, Province of Neuquen, and are listed in stratigraphic order (Ardolino et al., 1995). Symbols as in Fig. 2.

ultrasonically washed with deionized water and a 10% nitric acid solution. Heavy liquids were used to keep groundmass in narrow density ranges, and to remove phenocrysts and, if present, any slightly weathered fraction. A Frantz magnetic separator was used to further improve purity of the groundmass fraction. Both potassium and argon were measured in the GEOPS (Geosciences Paris Sud) laboratory at Orsay (France), on different aliquots of the same preparation. Potassium was measured by flame absorption spectroscopy and compared with MDO-G, ISH-G and BCR-2 (USGS) standards (Gillot et al., 1992). The relative uncertainty on K measurement is about 1% over a range of K contents between 0.1 and 15%. Argon (Ar) was measured by mass spectrometry using an instrument similar to the one described in Gillot and Cornette (1986), with a limit of detection of the radiogenic Ar content of 0.1% (Quidelleur et al., 2001), which allows ages as young as 2 ka to be obtained with only a few centuries uncertainty (Gillot et al., 2006). Calibration of the system is obtained by systematic measurements of an air pipette, which is routinely compared to the HD-B1 standard (Fuhrmann et al., 1987), with a recommended age of 24.21 ± 0.32 Ma (Hess and Lippolt, 1994), recently confirmed at 24.18 ± 0.09 Ma (Schwarz and Trieloff, 2007). Such a ^{40}Ar signal calibration introduces an additional relative uncertainty of 1%, which leads to a total relative age uncertainty of about 1.5% for a 1 Ma sample. Age calculations were performed using decay constant and K isotopic ratios of Steiger and Jäger (1977). All K and Ar measurements have been duplicated. The mean age and uncertainty (reported here at the 1σ level) have been calculated by weighting each analysis with the amount of ^{40}Ar*.

4. Results

4.1. Major and trace element composition

The new chemical analyzes from Auca Mahuida volcano are listed in Table 1. Our new data were combined with previously published data for the Auca Mahuida (Kay et al., 2006a, 2006b, 2013, 2004; Gudnason et al., 2012; Jacques et al., 2013. See caption in Fig. 4, for better understanding and interpretations). All these samples are relatively fresh, with loss on ignition (LOI) values about 1. K_2O vs SiO_2 (Peccerillo and Taylor, 1976) show that rocks from Auca Mahuida volcano plot along a single magmatic series between the high-K calc-alkaline and shoshonitic series (Fig. 4a). We also used the TAS diagram ($Na_2O + K_2O$ vs SiO_2 from Le Bas et al. (1986); Fig. 4b) more adapted for alkali magmas, there, the rocks plot in trachybasalt, basaltic trachyandesite, trachyandesite and trachyte fields.

Two out of the 23 newly collected samples from Auca Mahuida volcano are alkali basalts, 9 trachybasalts, 6 basaltic trachyandesites, 5 trachyandesites and only one is a trachyte (Fig. 4; Table 1). Alkali basalts are located in the Pampa de Las Yeguas and Pampa del Leon formations, while trachybasalts are distributed in several formations (La Faja,

Table 1
Chemical analyses of Plio-Pleistocene lavas from Auca Mahuida volcano. ICP-AES: Thermo Electron IRIS Advantage and Thermo Elemental X7 analyses according to the procedures used at CRPG. Fe_2O_3*: total iron as Fe_2O_3; LOI: loss on ignition; CIPW norm: q — quartz, an — anorthite, di — diopside, ne — nepheline, ol — olivine, hy — hypersthene; Mg# = Mg / (Mg + Fe^{2+}). CIPW norm and Mg# calculated with 15 at.% of total iron as Fe^{3+} and 85% as Fe^{2+}.

Sample	88AE	88AG	88AF	88AK	88AH	88AJ	88AI
Coordinates	37°44′54.60″S	37°46′1.12″S	37°45′53.53″S	37°47′23.11″S	37°46′13.41″S	37°46′50.20″S	37°46′43.62″S
	68°53′35.20″W	68°53′10.36″W	68°53′12.44″W	68°52′53.20″W	68°53′7.69″W	68°53′10.20″W	68°53′8.22″W
Rock type	Trachyandesite	Trachybasalt	Trachybasalt	Trachybasalt	Trachybasalt	Trachybasalt	Trachybasalt
Age (Ma)	1.26 ± 0.02	1.36 ± 0.02	1.17 ± 0.02	1.35 ± 0.02	1.40 ± 0.02	1.44 ± 0.02	
Major elements (wt.%)							
SiO_2	58.00	49.47	48.04	47.15	46.94	46.89	46.84
TiO_2	0.82	2.17	2.36	2.11	2.05	2.06	2.02
Al_2O_3	18.15	17.39	17.25	14.98	14.77	14.38	14.78
Fe_2O_3	6.35	10.28	11.71	11.64	11.69	12.02	11.42
FeO*	5.71	9.24	10.53	10.47	10.51	10.81	10.27
MnO	0.15	0.16	0.17	0.16	0.16	0.16	0.16
MgO	0.95	3.85	4.50	9.03	9.20	9.70	8.73
CaO	3.04	7.87	7.75	8.53	8.89	8.73	8.93
Na_2O	6.85	4.72	4.79	3.80	3.64	3.58	3.75
K_2O	3.94	2.13	1.83	1.59	1.36	1.40	1.50
P_2O_5	0.34	0.75	0.72	0.57	0.51	0.56	0.52
LOI	0.15	0.00	−0.07	−0.46	−0.29	−0.34	−0.04
Total	98.72	98.78	99.05	99.10	98.92	99.15	98.61
CIPW minerals							
q	0.00	0.00	0.00	0.00	0.00	0.00	0.00
an	7.27	20.35	20.50	19.36	20.27	19.29	19.48
di	4.89	11.67	11.21	15.78	16.95	16.74	17.87
ne	4.09	3.94	5.64	4.73	4.02	3.86	5.01
ol	2.74	6.38	8.90	16.09	16.32	17.61	15.03
hy	0.00	0.00	0.00	0.00	0.00	0.00	0.00
Mg#	22.86	42.60	43.23	60.58	60.94	61.53	60.24
Trace elements (ppm)							
Cs	3.12	1.32	0.58	0.49	0.57	0.89	0.64
Rb	97.2	46.4	31.8	26.4	23.0	25.7	25.2
Ba	579	471	389	303	285	291	286
W	1.68	0.54	0.38	0.40	0.41	0.34	0.38
Th	10.39	4.52	2.55	2.70	2.32	2.65	2.40
U	3.33	1.35	0.84	0.70	0.74	0.83	0.75
Nb	57.1	30.7	29.3	25.2	21.9	25.5	22.2
Ta	4.53	2.42	2.16	2.00	1.71	1.88	1.75
La	40.9	29.9	26.6	21.6	18.8	21.3	19.1
Ce	76.2	61.2	57.2	45.7	40.2	43.9	40.8
Pb	10.63	4.61	3.02	2.70	2.47	2.41	2.54
Pr	7.84	7.06	6.78	5.36	4.82	5.50	4.83
Mo	6.90	2.83	2.09	2.05	1.90	2.31	2.03
Sr	435	786	750	649	612	597	597
Nd	31.0	32.0	31.4	24.8	22.8	23.3	22.3
Sm	6.06	6.93	7.02	5.51	5.22	5.37	5.20
Zr	505	218	193	158	142	165	146
Hf	10.05	5.04	4.55	3.86	3.52	3.73	3.55
Eu	1.85	2.39	2.45	1.94	1.83	1.91	1.82
Sn	3.66	1.97	1.87	1.68	1.45	1.47	1.48
Gd	5.25	6.31	6.58	5.21	4.97	5.13	4.96
Tb	0.81	0.91	0.94	0.74	0.72	0.75	0.71
Dy	4.72	4.99	5.22	4.09	4.02	4.12	3.89
Y	26.6	25.6	26.6	20.2	19.9	20.2	19.5
Ho	0.89	0.90	0.95	0.71	0.71	0.72	0.70
Er	2.57	2.36	2.48	1.84	1.82	1.86	1.78
Tm	0.39	0.33	0.34	0.25	0.25	0.26	0.24
Yb	2.76	2.13	2.18	1.56	1.56	1.61	1.53
Lu	0.43	0.32	0.32	0.23	0.23	0.23	0.23
Sc	3.7	17.5	16.8	21.0	22.6	0.0	21.9
V	8	199	188	191	206	202	191
Cr	0	23	13	315	352	366	336
Co	4.8	26.7	32.3	45.9	48.3	50.7	44.6
Ni	0	21	22	195	203	227	189
Cu	6.7	33.1	35.2	45.1	50.6	46.9	48.0
Zn	116	109	122	105	104	114	100
Be	5.11	2.36	1.91	1.65	1.46	1.55	1.52
Ga	28.90	25.24	25.54	21.19	21.29	21.31	20.50
Ge	1.51	1.44	1.48	1.40	1.45	1.41	1.34
La/Nb	0.71	0.99	0.90	0.86	0.86	0.83	0.86
Ba/La	14.14	15.77	14.63	14.04	15.18	13.69	14.96
La/Yb	14.84	13.99	12.20	13.86	12.01	13.21	12.47

Table 1 (*continued*)

Sample	88AE	88AG	88AF	88AK	88AH	88AJ	88AI
Coordinates	37°44′54.60″S	37°46′1.12″S	37°45′53.53″S	37°47′23.11″S	37°46′13.41″S	37°46′50.20″S	37°46′43.62″S
	68°53′35.20″W	68°53′10.36″W	68°53′12.44″W	68°52′53.20″W	68°53′7.69″W	68°53′10.20″W	68°53′8.22″W
Rock type	Trachyandesite	Trachybasalt	Trachybasalt	Trachybasalt	Trachybasalt	Trachybasalt	Trachybasalt
Age (Ma)	1.26 ± 0.02	1.36 ± 0.02	1.17 ± 0.02	1.35 ± 0.02	1.40 ± 0.02	1.44 ± 0.02	
Ba/Th	55.79	104.08	152.84	112.13	122.95	109.80	119.19
Zr/Hf	50.28	43.25	42.40	41.04	40.32	44.22	41.10
Zr/Nb	8.84	7.10	6.57	6.29	6.48	6.46	6.57

Sample	AM8	AM31	AM45	AM70	AM7	AM33	AM50
Coordinates	37°44′7.44″S	37°46′22.92″S	37°45′49.92″S	37°46′18.12″S	37°44′14.28″S	37°46′22.92″S	37°44′43.92″S
	68°55′14.82″W	68°53′36.54″W	68°54′31.08″W	68°53′38.28″W	68°55′11.46″W	68°53′36.54″W	68°55′4.38″W
Rock type	Trachyte	Trachyandesite	Trachyandesite	Trachyandesite	Trachyandesite	Basaltic Trachyandesite	Basaltic Trachyandesite
Age (Ma)	1.48 ± 0.02						
Major elements (wt.%)							
SiO_2	61.89	58.21	58.15	54.69	53.72	52.88	52.37
TiO_2	0.52	0.47	0.80	1.38	1.44	1.51	1.95
Al_2O_3	18.15	17.01	18.6	17.69	18.15	17.91	17.11
Fe_2O_3	4.46	4.78	6.19	8.02	8.49	8.53	9.81
FeO*	4.01	4.30	5.57	7.21	7.64	7.67	8.83
MnO	0.15	0.11	0.14	0.13	0.15	0.13	0.14
MgO	0.62	0.6	1.06	2.52	2.31	3.90	3.53
CaO	2.10	2.21	3.52	4.91	4.64	6.91	7.33
Na_2O	6.65	4.27	6.58	5.19	5.91	5.01	4.91
K_2O	5.01	4.27	3.81	3.12	3.21	2.64	2.29
P_2O_5	0.29	0.26	0.36	0.54	0.72	0.56	0.65
LOI	0.19	7.76	0.74	1.76	0.81	−0.03	−0.13
Total	99.75	92.19	99.21	98.19	98.74	99.98	100.09
CIPW minerals							
q	0.00	11.99	0.00	0.00	0.00	0.00	0.00
an	4.89	10.08	10.08	16.13	13.76	18.69	17.98
di	3.04	0.00	4.35	4.24	4.02	9.77	11.61
ne	0.14	0.00	2.69	0.00	3.74	2.61	1.17
ol	1.35	0.00	2.97	2.62	6.31	6.84	5.75
hy	0.00	4.28	0.00	4.93	0.00	0.00	0.00
Mg#	21.59	19.91	25.33	38.37	35.03	47.54	41.62
Trace elements (ppm)							
Cs	1.70	4.30	1.90	2.00	1.80	0.50	0.60
Rb	92.8	145.0	96.0	72.6	78.4	44.8	44.9
Ba	643	273	577	635	668	527	565
W	0.80	3.00	2.20	1.90	2.80	3.90	2.20
Th	7.20	15.60	10.50	6.90	7.20	4.10	4.00
U	1.80	4.30	0.50	1.90	2.10	1.00	3.00
Nb	35.0	71.3	55.6	40.4	52.0	30.5	27.7
Ta	2.60	5.90	4.30	3.20	3.70	2.10	2.10
La	34.5	51.6	40.0	35.3	42.4	25.6	28.6
Ce	63.6	91.5	74.2	66.5	80.8	50.3	67.7
Pb	9.90	19.90	12.20	11.70	8.70	7.10	6.20
Pr	7.20	9.10	7.80	7.60	9.10	6.00	7.10
Mo	2.40	9.10	7.00	5.50	6.80	5.90	5.80
Sr	224	176	460	567	613	668	607
Nd	24.7	32.3	29.1	29.5	35.4	23.4	29.0
Sm	5.20	5.20	6.90	5.90	6.80	5.20	6.00
Zr	351	649	456	330	382	649	222
Hf	7.30	14.10	9.40	6.90	7.60	4.50	4.90
Eu	1.40	0.80	1.90	1.80	2.20	1.80	2.40
Sn	2.60	5.00	3.40	2.80	2.80	1.60	1.90
Gd	4.10	4.90	4.80	5.10	5.60	4.30	5.70
Tb	0.60	0.80	0.70	0.70	0.90	0.60	0.80
Dy	3.50	4.70	3.90	3.80	4.60	3.50	4.70
Y	20.0	29.4	25.7	21.5	24.7	19.8	23.8
Ho	0.70	0.90	0.80	0.70	0.80	0.70	0.80
Er	1.90	2.80	2.40	2.00	2.10	1.60	2.30
Tm	0.30	0.50	0.20	0.30	0.30	0.30	0.30
Yb	1.90	2.90	2.30	2.00	1.90	1.60	2.00
Lu	0.30	0.50	0.40	0.30	0.30	0.30	0.30
Sc	4.8	3.5	4.7	8.0	7.5	11.8	13.3
V	9	12	12	79	61	137	164
Cr	10	16	28	40	54	149	67
Co	2.9	3.6	5.6	10.6	13.4	22.9	23.7

(*continued on next page*)

Table 1 (*continued*)

Sample	AM8	AM31	AM45	AM70	AM7	AM33	AM50
Coordinates	37°44′7.44″S	37°46′22.92″S	37°45′49.92″S	37°46′18.12″S	37°44′14.28″S	37°46′22.92″S	37°44′43.92″S
	68°55′14.82″W	68°53′36.54″W	68°54′31.08″W	68°53′38.28″W	68°55′11.46″W	68°53′36.54″W	68°55′4.38″W
Rock type	Trachyte	Trachyandesite	Trachyandesite	Trachyandesite	Trachyandesite	Basaltic Trachyandesite	Basaltic Trachyandesite
Age (Ma)	1.48 ± 0.02						
Ni	3	5	6	20	12	38	22
Cu	8.0	18.6	9.2	22.4	18.9	25.1	26.1
Zn	83	649	456	114	128	104	119
Be	2.50	5.10	4.00	2.30	3.00	1.20	1.70
Ga	26.80	31.30	29.60	26.10	28.50	24.50	24.50
Ge	1.30	1.40	1.50	1.30	1.40	1.20	1.30
La/Nb	0.07	0.08	0.07	0.08	0.071	0.07	0.07
Ba/La	18.62	5.29	14.43	17.98	15.75	20.59	19.76
La/Yb	18.16	17.79	17.39	17.65	22.31	16.00	14.30
Ba/Th	89.25	17.49	54.97	91.98	92.79	128.56	141.32
Zr/Hf	67.50	124.77	66.09	55.88	56.16	124.75	37.01
Zr/Nb	10.03	9.10	8.20	8.16	7.34	21.26	8.02

Sample	AM71	AM28	AM66	AM26	AM52	AM37	AM79
Coordinates	37°42′10.86″S	37°48′11.52″S	37°45′11.10″S	37°44′13.80″S	37°48′12.60″S	37°51′29.22″S	37°48′3.60″S
	68°56′29.94″W	68°51′57.90″W	68°56′15.96″W	68°54′43.26″W	68°52′54.78″W	68°35′21.48″W	68°35′14.70″W
	Basaltic	Basaltic	Basaltic			Alkali	Alkali
Rock type	Trachyandesite	Trachyandesite	Trachyandesite	Trachybasalt	Trachybasalt	Basalt	Basalt
Age (Ma)			1.30 ± 0.02		1.61 ± 0.02		
Major elements (wt.%)							
SiO_2	52.37	51.79	51.78	48.77	47.81	47.31	47.22
TiO_2	1.64	1.69	1.96	1.84	1.86	2.11	2.00
Al_2O_3	19.67	19.23	17.31	17.67	13.82	15.12	15.11
Fe_2O_3	7.75	8.46	10.62	10.13	12.03	11.02	12.53
FeO*	6.97	7.61	9.55	9.11	10.82	9.91	11.27
MnO	0.12	0.12	0.16	0.13	0.15	0.14	0.16
MgO	2.97	3.06	3.21	5.19	10.80	7.87	8.40
CaO	7.60	7.89	6.05	9.17	8.45	9.62	9.31
Na_2O	5.10	4.79	5.46	4.46	3.69	3.66	3.48
K_2O	2.12	2.04	2.32	1.51	1.36	1.18	0.95
P_2O_5	0.71	0.74	0.80	0.66	0.58	0.54	0.59
LOI	−0.10	0.12	0.27	0.19	−0.60	1.37	0.60
Total	100.05	99.82	99.67	99.53	100.55	98.57	99.75
CIPW minerals							
q	0.00	0.00	0.00	0.00	0.00	0.00	0.00
an	24.62	25.12	16.04	24.01	17.18	21.81	23.07
di	6.88	7.62	7.38	14.24	16.87	18.69	15.93
ne	1.85	0.91	2.83	4.80	3.68	2.85	1.37
ol	4.80	5.44	7.72	8.62	19.89	12.39	16.33
hy	0.00	0.00	0.00	0.00	0.00	0.00	0.00
Mg#	43.16	41.75	37.46	50.38	64.02	58.60	57.06
Trace elements (ppm)							
Cs	1.20	0.70	0.90	0.60	0.50	0.30	0.40
Rb	45.8	41.5	48.6	28.2	30.5	18.0	19.2
Ba	546	554	605	296	353	286	290
W	2.30	2.30	3.30	4.40	2.20	2.10	2.30
Th	4.30	4.20	4.90	2.30	2.70	2.00	1.50
U	1.10	1.10	1.40	0.60	0.80	0.50	0.40
Nb	29.4	28.9	38.9	22.5	25.9	22.6	18.1
Ta	2.10	2.00	2.80	1.40	1.80	1.500	1.20
La	29.8	30.4	35.4	21.1	22.0	17.1	14.9
Ce	59.5	56.6	70.0	42.7	44.0	38.8	33.9
Pb	7.00	6.60	7.70	5.70	6.30	4.80	3.90
Pr	6.60	7.20	9.00	5.30	5.60	4.90	4.30
Mo	4.30	20.00	6.50	6.30	4.20	3.30	3.90
Sr	964	628	626	676	658	692	633
Nd	27.3	28.8	35.5	22.7	24.2	21.6	19.9
Sm	5.70	5.20	7.90	5.10	5.30	5.10	5.20
Zr	203	212	282	155	145	142	124
Hf	4.10	4.60	6.10	3.30	3.40	3.30	2.90
Eu	2.10	2.10	2.00	1.70	1.80	1.70	1.70
Sn	1.90	2.00	2.30	1.60	1.50	1.40	1.40
Gd	4.60	5.10	7.40	4.70	4.50	4.70	5.00
Tb	0.70	0.80	1.00	0.70	0.70	0.70	0.70
Dy	3.60	4.00	5.40	3.90	3.80	4.00	3.70

Table 1 (*continued*)

Sample	AM71	AM28	AM66	AM26	AM52	AM37	AM79
Coordinates	37°42′10.86″S	37°48′11.52″S	37°45′11.10″S	37°44′13.80″S	37°48′12.60″S	37°51′29.22″S	37°48′3.60″S
	68°56′29.94″W	68°51′57.90″W	68°56′15.96″W	68°54′43.26″W	68°52′54.78″W	68°35′21.48″W	68°35′14.70″W
	Basaltic	Basaltic	Basaltic			Alkali	Alkali
Rock type	Trachyandesite	Trachyandesite	Trachyandesite	Trachybasalt	Trachybasalt	Basalt	Basalt
Age (Ma)			1.30 ± 0.02		1.61 ± 0.02		
Y	20.6	23.7	30.3	22.0	19.3	19.9	20.1
Ho	0.70	0.80	1.10	0.70	0.70	0.70	0.70
Er	1.80	2.00	2.70	1.90	1.70	1.70	1.60
Tm	0.20	0.30	0.40	0.30	0.20	0.20	0.30
Yb	1.60	1.80	2.70	1.60	1.40	1.40	1.60
Lu	0.20	0.30	0.40	0.20	0.20	0.20	0.20
Sc	10.6	11.6	11.3	15.1	16.6	16.6	16.7
V	116	127	93	179	181	204	197
Cr	72	71	66	176	450	330	311
Co	19.0	20.0	20.2	31.9	54.4	43.6	50.6
Ni	27	18	11	43	279	146	172
Cu	28.3	33.2	22.6	79.0	54.2	42.7	51.5
Zn	97	105	141	106	122	142	126
Be	2.00	1.60	2.10	1.00	1.00	1.20	1.20
Ga	25.40	26.20	27.10	23.40	20.70	21.10	21.90
Ge	1.30	1.10	1.50	1.30	1.20	1.20	1.40
La/Nb	0.07	0.07	0.07	0.06	0.07	0.06	0.06
Ba/La	18.32	18.22	17.09	14.01	16.03	16.72	19.47
La/Yb	18.62	16.88	13.11	13.19	15.71	12.21	9.31
Ba/Th	126.95	131.90	123.51	128.52	130.59	143.00	193.40
Zr/Hf	35.70	40.84	35.73	30.33	27.34	27.84	23.92
Zr/Nb	6.92	7.35	7.26	6.87	5.59	6.28	6.87

Rincon del Infiernillo, Pampa del Leon and Aguada Lastras). Basaltic trachyandesites belong to the La Faja, Rincon del Infiernillo, Pampa del Leon and Auca Mahuida formations, whereas trachyandesites come mainly from Puesto Retamal and only one from the Auca Mahuida formation. Finally, the only trachyte belongs to the Auca Mahuida formation.

Incompatible trace elements (Table 1) are shown in Fig. 5 as multi-element patterns normalized to the primitive mantle (PM; a) and to the chondrites (CH; b) of Sun and McDonough (1989). Auca Mahuida basaltic magmas show moderately fractionated patterns and a slight depletion in heavy REE and Y, as well as no significant depletion in Nb. These lavas also show positive anomalies in some of the most incompatible elements (Cs, Ba, U, K, Sr), Pb, P, and Ti and negative anomalies in Rb, Th, Nd, and to a lesser extent in light rare earth elements (La, Ce) can be observed. Trachyandesites and trachytes displays a pattern rather similar to that of the trachybasalts, although they show a marked increase of incompatible elements Pb and Zr, as well as a significant decrease of Sr, P, Eu and Ti (Fig. 5a). The pattern of rare earth elements (REE) is enriched in light rare earth elements (LREE) and slightly enriched in middle rare earth elements (MREE). Some basaltic samples from previous studies show negative anomalies in Pr and Gd, while only one trachyte is depleted in Eu (Fig. 5b). Here, Pr and Gd negative anomalies (samples AU4 and RD17 from Kay et al. (2013)) are probably due to analytical problems.

Element concentration ratios from Auca Mahuida lavas, normalized to the primitive mantle (Sun and McDonough, 1989), such as Th/Nb, K/Nb, and La/Nb (not shown), are very close to unity. Such a feature and the high contents in Nb observed for these lavas (Table 1) are consistent with an OIB-type geochemical affinity. This is also supported by the rather flat patterns displayed in the multi-element diagrams (Fig. 6) when normalized to OIB-type rock from Sun and McDonough (1989).

4.2. Petrology

Some authors, such as Ardolino et al. (1995) and Kay et al. (2013), have conscientiously described the mineralogy, petrography and petrology of Auca Mahuida in the past, thus in this work, we only aim at completing their research. Samples from Auca Mahuida volcano can be separated into different fields based on their MgO content (Fig. 7 and Table 1). Rocks with MgO contents higher than 8 wt.% will be referred as primitive basalts (red area), those with MgO contents between 8 and 5% as evolved basalts (orange area), and those with MgO contents from 5 to 3 wt.% as basaltic-andesites (yellow area). In addition, trachytic rocks display a MgO value lower than 3 wt.% (Fig. 7). Overall, the two main groups can be defined using a cut-off value of 8 wt.% for their MgO content. The high-MgO group includes both alkali basalts and trachybasalts, while the low-MgO group includes evolved trachybasalts and basaltic trachyandesites (Table 1 and Fig. 7).

The petrographic features of alkali basalts show a microlitic–porphyritic texture where phenocrysts of olivine are predominant (>10%), and plagioclase and clinopyroxene (augite) are less abundant. Apatite is sometimes an accessory mineral, and chlorite and Fe-oxides form some altered minerals produced by the destabilization of olivine and Fe–Mg–Ti minerals.

The trachybasaltic rocks analyzed here show a dark gray color and have a fine grained (aphanitic) texture, but rare phenocrysts such as olivine, pyroxene and plagioclase from about 1 to 2 mm can be found. Despite their density and compaction, several small (≤1 mm) and big vesicles (1–5 mm) are present, with the latter often filled with carbonates or zeolitic minerals. The disposition of vesicles is random, but in some samples, such as 88AG, they are elongated and preferentially aligned. In thin section, the texture of the high-MgO samples, such as 88AI, 88AJ, 88AH or 88AK (Fig. 6) from the Rincón del Infiernillo formation, varies from hypocrystalline to middle holocrystalline, slightly doleritic, inequigranular, and slightly intersertal microporphyritic. These rocks consist mainly of euhedral–subhedral elongated-acicular plagioclase (bytownite–labradorite) of about 0.2 mm, many subhedral wrapped round small olivine crystals (about 0.1 mm) and other euhedral–subhedral plagioclase and olivine phenocrysts varying from 0.2 to 2 mm, some subhedral–anhedral clinopyroxene (augite) and rare leucite. The interstices are filled with smaller plagioclase, olivine

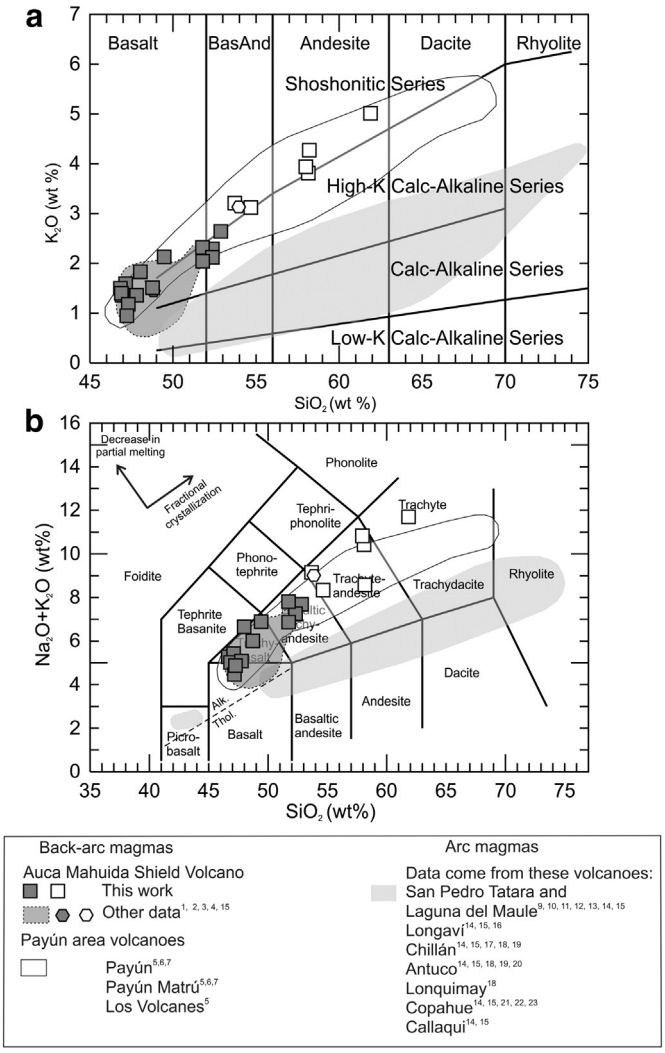

Fig. 4. (a) K_2O–SiO_2 and (b) total-alkali-silica (TAS) plots for the studied lavas, according to Peccerillo and Taylor (1976) and Le Bas et al. (1986) respectively. The dotted line separating the fields of tholeiitic (Thol.) and alkali (Alk.) basalts is from Macdonald and Katsura (1964). Geochemical data are from: [1]Kay et al. (2006a), [2]Kay et al. (2006b), [3]Kay et al. (2004), [4]Kay et al. (2013), [5]Gudnason et al. (2012), [6]Germa et al. (2010), [7]Søager et al. (2013), [8]Hernando et al. (2014a,b), [9]Debreil et al. (work in progress), [10]Frey et al. (1984), [11]Ferguson et al. (1992), [12]Feeley et al. (1998), [13]Costa and Singer (2002), [14]Dungan et al. (2001), [15]Stern (2004), [16]Jacques et al. (2013), [17]Rodríguez et al. (2007), [18]Dixon et al. (1999), [19]Deruelle (1982), [20]Deruelle and Lopez-Escobar (1999), [21]Lopez-Escobar et al. (1981), [22]Muñoz and Stern (1988), [23]Muñoz et al. (1989), [24]Varekamp et al. (2006).

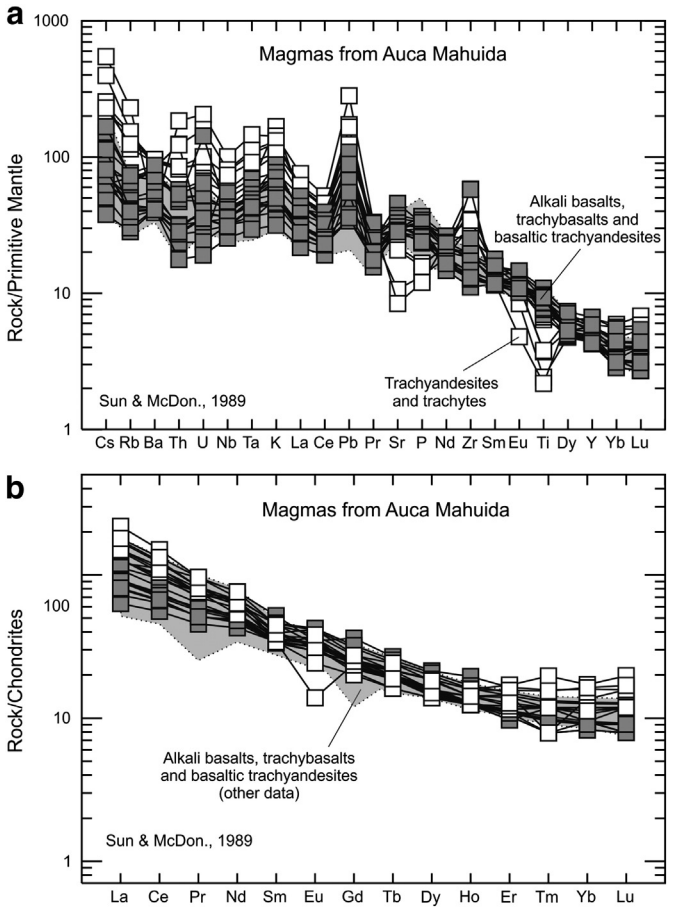

Fig. 5. Incompatible multi-element patterns of selected Plio-Quaternary lavas normalized to the Primitive Mantle of Sun and McDonough (1989). Symbols as in Fig. 4.

and Fe–Ti minerals. Petrographically, they can be referred to as olivine basalts.

The low-MgO samples, such as 88AG and 88AF, clearly show a decrease of the content in Fe–Mg minerals (Fig. 6). Their texture in thin section is principally hypocrystalline, inequigranular, microporphyritic, or seriate. Some samples, such as 88AF (Fig. 6), display an aligned or oriented texture, highlighting a fluidal orientation of plagioclase microcrystals. The main minerals consist in subhedral elongated-acicular anorthite–bytownite of about 0.2 mm, and euhedral columnar labradorite that reached up to a 5 mm size, abundant subhedral round small olivine (about 0.1 mm) and bigger olivine crystals varying between 0.2 and 1 mm, some phenocrysts of clinopyroxene with an approximate size of 5 mm. The interstices are filled with much smaller plagioclase, olivine and Fe–Ti minerals. These rocks can be described as seriate-textured basalts.

The basaltic trachyandesites from the low-MgO content group show microlitic and microporphyritic textures. The prevailing phenocrysts are plagioclase (andesine–oligoclase), with some olivines, clinopyroxene, anorthoclase, a few amphibole and Fe–Ti minerals. The groundmass is generally composed of the same minerals, however, without any relationship, the proportion of plagioclase seem to increase when Fe–Mg mineral content decreases. Apatite is sometimes present as an accessory mineral. The Fe-oxides and chlorite (rare) represent alteration-related minerals, probably formed by destabilization of Fe–Mg and Fe–Ti minerals.

Textures of trachyandesitic rocks are heterogeneous and vary from microlitic to microporphyritic, but glassy ones are also observed. Some minerals such as plagioclase and anorthoclase are abundant, while olivine, clinopyroxene, amphibole and Fe–Ti minerals are less abundant. For example, the macroscopic features of the trachyandesite 88AE are a gray color and a homogeneous matrix, but some phenocrystals such as feldspar and amphibole are observable. The size of feldspars reaches up to 5 mm (rarely up to 1 cm) whereas amphiboles are less than 1 mm. Some small vesicles exist and are dispersed within the groundmass of massive and moderately-dense trachyandesite. And the microscopic features of 88AE shown in thin section (Fig. 6) reveal hypohyaline, inequigranular, porphyritic, seriate and slightly glomeroporphyritic textures. The matrix is mostly composed with microcrystals of plagioclase, pyroxene and Fe–Ti minerals. Among the most important minerals, we distinguish subhedral small olivine, plagioclase, anorthoclase and pyroxene (<0.5 mm), and rare euhedral elongated labradorite between 0.2 and 1 cm.

The only trachyte analyzed here (AM8; Table 1) is characterized by a microporphyritic texture with abundant phenocrysts of plagioclase and anorthoclase, minor amphibole (perhaps kaersutite) and Fe–Ti minerals, and rare clinopyroxene. The whitish groundmass is essentially composed of an intergrowth of predominant anorthose with less

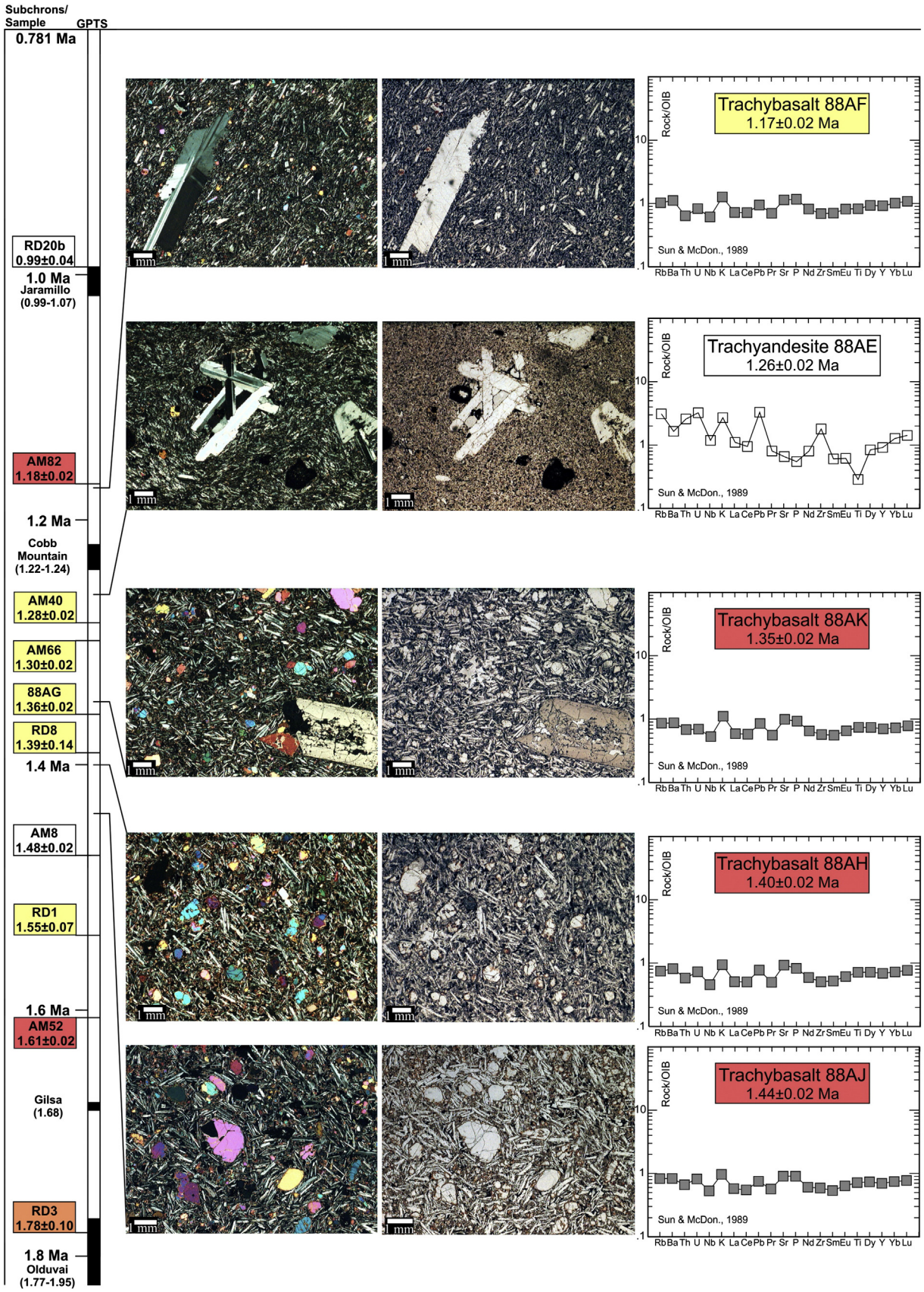

Fig. 6. Chronostratigraphical correlation and major petrographic characteristics of basaltic and andesitic rocks from Auca Mahuida shield volcano. Right panels are normalized to the OIB of Sun and McDonough (1989). The left side pictures were taken in polarized light, and those on the right side were taken in natural light, with a magnification of ×10. Red field: primitive basalts; orange field: evolved basalts; light yellow field: basaltic–andesitic rocks; white field: trachytic rocks. (For interpretation of the references to color in this figure legend, the reader is referred to the online version of this chapter.)

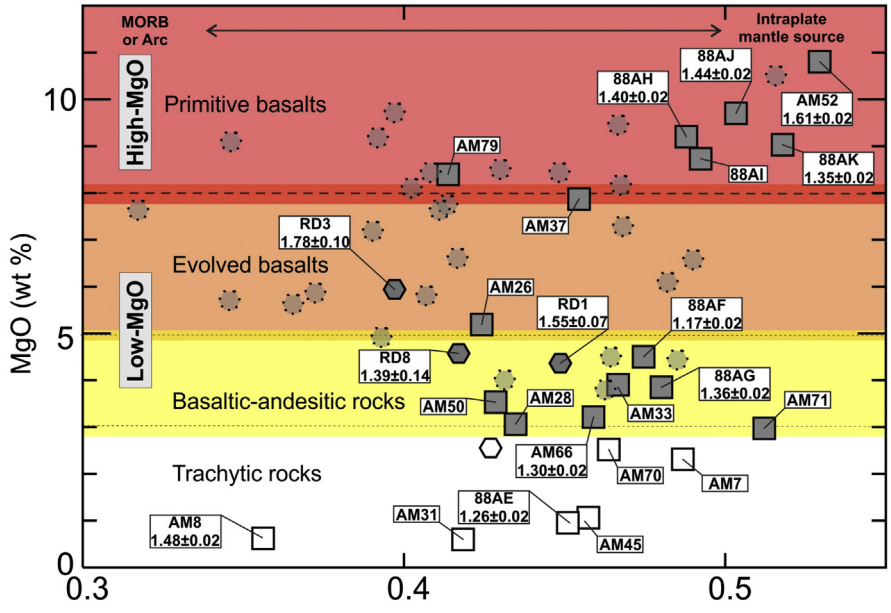

		Sample	Age	Rock type	Formation
Phase 5 younger	27	RD20b	0.99 ± 0.04	Trachyandesite	Puesto Retamal
	26	88AF	1.17 ± 0.02	Trachybasalt	Aguada Lastra Volcanics
	25	AM82	1.18 ± 0.02	Trachybasalt	Pampa del Leon
Phase 4	24	AM31		Trachyandesite	Puesto Retamal
	23	88AE	1.26 ± 0.02	Trachyandesite	Puesto Retamal
	22	AM45		Trachyandesite	Puesto Retamal
	21	AM7		Trachyandesite	Auca Mahuida
	20	AM70		Trachyandesite	Puesto Retamal
	19	AM66	1.30 ± 0.02	Basaltic trachyandesite	Auca Mahuida
	18	AM50		Basaltic trachyandesite	Auca Mahuida
	17	AM33		Basaltic trachyandesite	Rincon del Infiernillo
	16	88AK	1.35 ± 0.02	Trachybasalt	Rincon del Infiernillo
Phase 3	15	88AG	1.36 ± 0.02	Trachybasalt	Rincon del Infiernillo
	14	RD8	1.39 ± 0.14	Basaltic trachyandesite	Cerro Grande
	13	AM28		Basaltic trachyandesite	Pampa del Leon
	12	AM40	1.40 ± 0.02	Basaltic trachyandesite	Pampa del Leon
	11	AM79		Alkali basalt	Pampa del Leon
	10	88AI		Trachybasalt	Rincon del Infiernillo
	9	88AH	1.40 ± 0.02	Trachybasalt	Rincon del Infiernillo
	8	88AJ	1.44 ± 0.02	Trachybasalt	Rincon del Infiernillo
Phase 2	7	AM8	1.48 ± 0.02	Trachyte	Auca Mahuida
	6	AM71		Basaltic trachyandesite	La Faja
	5	RD1	1.55 ± 0.07	Trachybasalt	Las Liebres
	4	AM52	1.61 ± 0.02	Trachybasalt	La Faja
Phase 1 older	3	AM26		Trachybasalt	La Faja
	2	RD3	1.78 ± 0.10	Trachybasalt	Pampa de Las Yeguas
	1	AM37		Alkali basalt	Pampa de Las Yeguas

Fig. 7. Top: MgO (wt.%) vs Ta/Hf ratio diagram showing the main affinities (MORB-Arc and intraplate) of mantle sources of the high-MgO basalts (primitive basalts), low-MgO basalts (evolved basalts and basaltic–andesitic rocks) and trachytic rock. Bottom: Chronologic and stratigraphic features of the five volcanic-phases identified in Auca Mahuida volcano. Red field: primitive basalts, orange field: evolved basalts, light yellow field: basaltic–andesitic rocks, white field: trachytic rocks. Ages from this study, except samples RD3, RD1, RD8 and RD20b (Kay et al., 2006a). (For interpretation of the references to color in this figure legend, the reader is referred to the online version of this chapter.)

abundant green clinopyroxenes, Fe–Ti minerals and rare mica. Fe–Ti minerals are destabilized in hematite. In addition, some microliths, such as apatite and quartz, seem present.

The CIPW normative mineral contents from Auca Mahuida rocks point to basaltic magmas with a high silica-undersaturated nature, where nepheline (ne) could be higher than 5% (Table 1 and Fig. 8). The olivine (ol) values in the high-MgO rocks from Rincón del Infiernillo and those from Aguada Lastra Volcanics vary from 15.03 to 17.61 while diopside (di) is given between 15.78 and 17.87. Anorthite (an; between 17.98 and 24.62) values are homogenous in basaltic–andesitic samples, except for evolved rocks that have 7.27. The CIPW normative mineral diagrams from the literature indicate that a lot of back-arc samples plot in alkali basalts and basanite fields (Thompson, 1984; Yoder and Tilley, 1962), as observed for our samples (Fig. 8). However, previous data from Auca Mahuida volcano and Payún area volcanoes also erupted some olivine tholeiites (Fig. 8). Note that silica-saturated or oversaturated rocks, also common in OIB-type magmatism, have not been found here (Table 1).

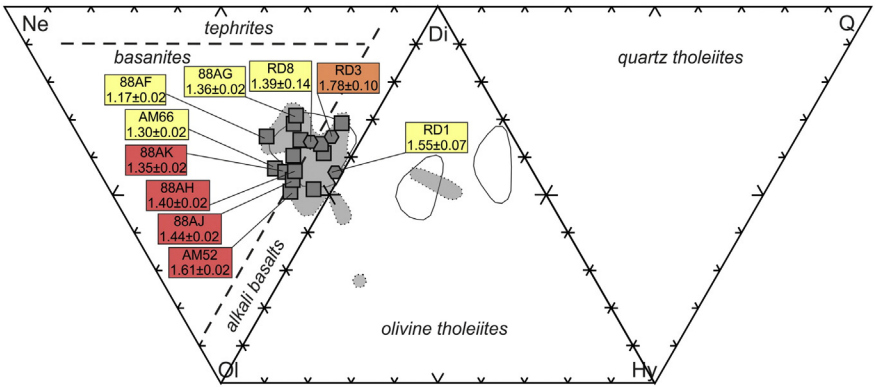

Fig. 8. CIPW normative mineral classification diagram of mafic lavas from back-arc alkali magmas. After Thompson (1984) and Yoder and Tilley (1962). CIPW norm is from Irvine and Baragar (1971). Same symbols as in Figs. 2 and 4.

4.3. K–Ar dating

The new ages obtained for Auca Mahuida volcano are reported in Table 2. All analyses have highly reproducible duplicates, highlighting the freshness of the rocks and the homogeneity of the mineralogical preparation. The relatively high K and radiogenic ($^{40}Ar^*$) contents (from 0.81 to 3.85% and from 5.4 to 38.5%, respectively; Table 2) made these samples quite straightforward for the K–Ar Cassignol–Gillot technique (Gillot et al., 2006). Our new ages for the Auca Mahuida shield volcano range between 1.17 ± 0.02 and 1.61 ± 0.02 Ma (Table 2).

5. Discussion

5.1. Comparison with previous ages available for the Auca Mahuida volcano

Several radiometric ages for the Auca Mahuida lavas were previously available. However, the reliability of some of them is subject to caution. Three whole-rock K–Ar ages ranging from 1.16 ± 0.09 to 1.52 ± 0.21 Ma are reported only in an unpublished abstract (Bermúdez et al., 2000), which prevents any assessment of the quality of these data. Furthermore, because whole-rock ages are often biased by slight alteration, and/or excess argon carried by mafic phenocrysts (e.g., Samper et al., 2008; Germa et al., 2011), we prefer not to consider further these three whole-rock K–Ar ages. Rossello et al. (2002) obtained eleven $^{40}Ar/^{39}Ar$ ages ranging from 0.88 ± 0.03 to 1.7 ± 0.2 Ma. Unfortunately, neither a detail regarding the analytical method nor a figure showing the age spectra or the inverse isochron is provided. Results are shown only as a table with plateau, isochron and preferred ages, when given. Without any justification provided, the preferred age is the plateau age in 5 out of 11 cases, while in 3 cases it is the isochron age. Surprisingly, although neither a plateau nor isochron ages are listed, a preferred age is given for two other samples. Because these data appear clearly unsupported, we cannot take into account these ages published by Rossello et al. (2002). Finally, four $^{40}Ar/^{39}Ar$ ages obtained on groundmass (RD1, RD3, RD8 and RD20; Fig. 2) have been obtained by Kay et al. (2006a). The age spectra display relatively flat plateaus, except for RD8, which shows decreasing apparent ages at high temperature steps; its age of 1.39 ± 0.14 Ma should therefore be considered as a minimum value. Samples RD1 and RD20 have plateau ages of 1.55 ± 0.07 and 0.99 ± 0.04 Ma, respectively. Sample RD3 has a relatively flat spectrum, and, as specified in Table 2 and in the text of Kay et al. (2006a), the age is 1.78 ± 0.07 Ma. Finally, note that since publication, the ages of the flux-monitors have been revised (e.g., Kuiper

Table 2
K–Ar ages of Auca Mahuida volcanic rocks. Column headings indicate sample names, geographic coordinates (lat.: latitude; long.: longitude), potassium (K) concentration in percent, concentration of radiogenic ^{40}Ar ($^{40}Ar^*$) in percent, concentration of radiogenic ^{40}Ar ($^{40}Ar^*$) $\times 10^{12}$ in number of atoms per gram, age ±1-sigma uncertainty (in Ma), mean age ±1-sigma uncertainty (in Ma) for each sample.

Sample	Phase	Lat. S	Long. W	K (%)	$^{40}Ar^*$ (%)	$^{40}Ar^*$ ($\times 10^{12}$ at/g)	Age ±1σ (Ma)	Mean age ±1σ (Ma)
88AF	Groundmass	37°45′53.53″	68°53′12.44″	1.58	30.0	1.945	1.18 ± 0.02	
					23.7	1.913	1.16 ± 0.02	**1.17 ± 0.02**
AM82	Groundmass	37°42′36.00″	68°53′17.22″	0.81	12.1	9.966	1.17 ± 0.02	
					13.2	1.009	1.19 ± 0.02	**1.18 ± 0.02**
88AE	Groundmass	37°44′54.60″	68°53′35.20″	3.83	28.3	5.080	1.27 ± 0.02	
					38.5	5.000	1.25 ± 0.02	**1.26 ± 0.02**
AM40	Groundmass	37°47′40.80″	68°52′29.40″	2.03	34.4	2.711	1.28 ± 0.02	
					32.4	2.717	1.28 ± 0.02	**1.28 ± 0.02**
AM66	Groundmass	37°45′11.10″	68°56′15.96″	2.38	21.1	3.160	1.27 ± 0.02	
					16.6	3.299	1.32 ± 0.02	**1.30 ± 0.02**
88AK	Groundmass	37°47′23.11″	68°52′53.20″	1.53	5.4	2.147	1.34 ± 0.03	
					15.0	2.163	1.35 ± 0.02	**1.35 ± 0.02**
88AG	Groundmass	37°46′1.12″	68°53′10.36″	1.80	25.3	2.528	1.35 ± 0.02	
					22.5	2.549	1.37 ± 0.02	**1.36 ± 0.02**
88AH	Groundmass	37°46′13.41″	68°53′7.69″	1.21	22.3	1.773	1.40 ± 0.02	
					16.7	1.766	1.40 ± 0.02	**1.40 ± 0.02**
88AJ	Groundmass	37°46′50.20″	68°53′10.20″	1.37	16.8	2.053	1.43 ± 0.02	
					12.5	2.081	1.45 ± 0.02	**1.44 ± 0.02**
AM8	Feldspars	37°44′7.44″	68°55′14.82″	3.85	38.3	5.919	1.47 ± 0.02	
					34.7	6.009	1.49 ± 0.02	**1.48 ± 0.02**
AM52	Groundmass	37°48′12.60″	68°52′54.78″	1.38	38.0	2.302	1.61 ± 0.02	
						2.229	1.61 ± 0.02	**1.61 ± 0.02**

et al., 2008) and are now at least 1% older. In the absence of mention of the flux-monitor and age used, no correction can be applied, but we can only point out that the ages of RD1, RD3, RD8 and RD20 as published by Kay et al. (2006a) are probably slightly underestimated.

Fig. 3 shows that the four previous ages selected here belong to the stratigraphic units of Pampa de León Basalt (RD1; trachybasalt), Pampa de las Yeguas Basalt (RD3; trachybasalt), Cerro Grande Basalt (RD8; basaltic trachyandesite) and Puesto Retamal Trachyandesite (RD20b; trachyandesite). They are located at the SW, S and E ends of the shield volcano (RD3, 1 and 8, respectively) and one is located close to the central caldera (RD20). Therefore, they complete nicely our own sampling, which is mainly focused on the central part of the shield volcano (Figs. 2 and 3). The complete data set displays ages ranging from 1.78 ± 0.07 to 0.99 ± 0.04 Ma, with an apparent major phase of activity between 1.2 and 1.5 Ma (Fig. 7).

5.2. Construction of the Auca Mahuida shield volcano

Integrating the new and previous reliable ages (see Section 5.1), stratigraphy (Ardolino et al., 1995), petrography, rock type and MgO contents, a high-resolution time-scale can be constructed for the 27 lavas investigated here (Fig. 7). Five main phases of volcanic activity can be identified for Auca Mahuida volcano from 1.78 ± 0.10 to 0.99 ± 0.04 Ma. Except for the oldest phase, for which basal lavas might be lacking here, each of them is initiated by the emission of high-MgO trachybasalts, which evolved toward more differentiated products, such as trachyandesites or trachytes (Fig. 7).

The first volcanic phase started at or slightly before 1.78 ± 0.10 Ma (Kay et al., 2006a; Fig. 7). The lavas outcropping today are only found at the periphery of the shield volcano and are evolved basalts (alkali and trachybasalts; Fig. 7) from Pampas de las Yeguas and La Faja formations (Fig. 3 and 7). These rocks belong to the low-MgO group, although sample AM37 is close to the boundary with the high-MgO content group (Fig. 7), and hence was supposed to be our oldest rock (as also supported by geochemical data; see Section 5.3 and Fig. 11).

The second volcanic phase identified here was erupted between 1.61 ± 0.02 and 1.48 ± 0.02 Ma (Fig. 7). This phase shows a noticeable evolution from a high-MgO trachybasalt (AM52) to a low-MgO trachyte (AM8). It ended the building of the central portion of La Faja formation, includes the peripheral Las Liebres basalts, and represents the oldest manifestation of the Auca Mahuida trachyandesite formation (AM8; Figs. 3 and 7).

The third volcanic phase was erupted between 1.44 ± 0.02 and 1.36 ± 0.02 Ma, and built the Rincon del Infiernillo, Pampa del Leon, and Cerro Grande formations (Figs. 3 and 7). The trachybasalts from Rincon del Infiernillo (samples 88AJ, 88AH, 88AI), which are primitive basalts from the high-MgO group, reveal an intense magmatic activity mainly located throughout the Rincon del Palo Blanco canyon between 1.44 ± 0.02 and 1.40 ± 0.02 Ma. Eruption of lavas from the high-MgO group also occurred in the peripheral zone, as shown by sample AM79 from the Pampa del Leon basalt (Figs. 3 and 7). Lavas from this formation then evolved to basaltic trachyandesite from the low-MgO group at 1.40 ± 0.02 Ma (Fig. 7). To the eastern end of the volcano, the Cerro Grande lavas were emitted at 1.39 ± 0.14 Ma (sample RD8), while coeval activity was present at 1.36 ± 0.02 Ma (sample 88AG) in Rincon del Infiernillo formation (Figs. 3 and 7).

The fourth volcanic phase started at 1.35 ± 0.02 Ma (sample 88AK), still in Rincon del Infiernillo formation. Lavas from the same formation but with lower MgO content were then erupted (sample AM33). The low-MgO content magmatic activity pursued with the emplacement of the Auca Mahuida formation at 1.30 ± 0.02 Ma (sample AM66). Then, basaltic–trachyandesitic magmatism evolved entirely to trachyandesitic, within the same Auca Mahuida group (sample AM7), and was followed by the eruption of the Puesto Retamal formation at about 1.26 ± 0.02 Ma (sample 88AE).

The fifth, and probably the youngest volcanic phase of Auca Mahuida volcano, includes three of the previously proposed (Ardolino et al., 1995) stratigraphic formations: Pampa del Leon, Aguada Lastra, and Puesto Retamal. Around 1.18 ± 0.02 Ma (sample AM82) a high-MgO volcanic activity resumed and built the recent trachybasaltic lavas from the Pampa del Leon formation. Lavas from the low-MgO group belonging to the Aguada Lastra Volcanics formation were then erupted at about 1.17 ± 0.02 Ma (88AF). Finally, the last reported activity of the Auca Mahuida volcano is the eruption of trachyandesite lava from the Puesto Retamal dated at 0.99 ± 0.04 Ma (sample RD20b; Kay et al., 2004, 2006a).

Although we did not date each stratigraphic formation identified by Ardolino et al. (1995), our radiometric data together with petrologic characterization show an overall good agreement with this previously proposed stratigraphy. However, our study shows that some stratigraphic formations had two or more volcanic phases, with marked geochemical variations through time (Fig. 7).

5.3. Magmatic evolution of Auca Mahuida lavas

The Ta/Hf ratio, shown in Fig. 7 as a function of MgO content, can be used to discriminate between MORB-Arc or intraplate mantle source magmatic affinities (Kay et al., 2006a, 2013). High Ta/Hf ratios reflect an OIB-like chemical signature in the olivine alkali basalts, while low Ta/Hf ratio can be associated with arc magmatism. Analyses of lavas from the active SVZ arc showed that the cut-off value is about 0.15 (Kay et al., 2006a). Clearly, as all new and previous rocks from the Auca Mahuida volcano display Ta/Hf values higher than 0.3, most being higher than 0.4, these rocks can be associated with an intraplate mantle source, as previously inferred (e.g., Kay et al., 2006a, 2013).

The high-MgO rocks from Auca Mahuida (Table 1) display contents of Co as low as 43 ppm, Cr up to 311 ppm, but slightly above 195 ppm for Ni (Cr up to 448 ppm, and Ni to 292 reported by Kay et al., 2013 for basaltic samples RD17, RD10, AU4): these values could rule out the hypothesis that such magmas originate from primitive liquids in equilibrium with a lherzolitic mantle source, but likely they were extracted from their mantle source by decompression melting (Kay et al., 2013) as a product extracted from a lherzolitic mantle (Allègre et al., 1977; Villemant et al., 1981; Pichavant et al., 2002).

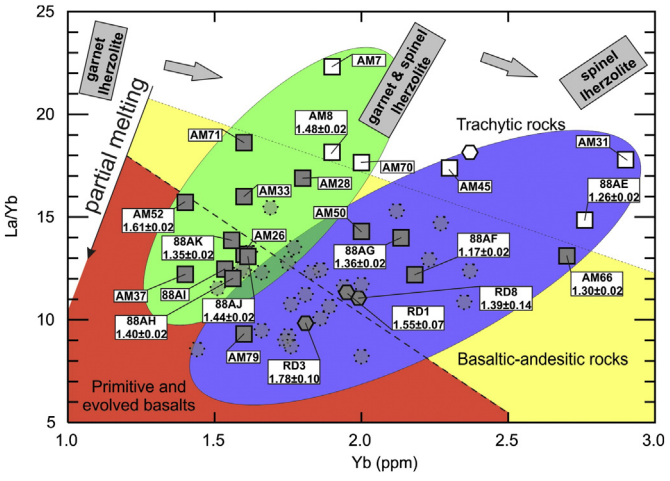

Fig. 9. La/Yb ratio vs Yb (ppm) diagram showing the partial melting trend and the likely mantle sources with their possible mantle mineralogy. Fractional crystallization would yield trends from the bottom left hand side to the top right hand side. Dark orange field: primitive basalts and evolved basalts; light yellow field: basaltic–andesitic rocks; white field: trachytic rocks, green field: lherzolite source with more garnet than spinel; blue field: lherzolite source with more spinel than garnet. (For interpretation of the references to color in this figure legend, the reader is referred to the online version of this chapter.)

Because La is highly incompatible, it is preferentially partitioned into the melt resulting from a low rate partial melting of a lherzolitic source. On the contrary, Yb being less incompatible than La is gradually incorporated, together with other HREE, in garnet. Thus, the La/Yb ratio then records variations of the partial melting rates (Luhr et al., 1995) in the source of the Auca Mahuida lavas (Fig. 9). Therefore, an Yb content decrease reveals a transition of the magmatic source from spinel-bearing lherzolite to garnet-bearing lherzolite. Therefore, it can be inferred from Fig. 9 that the Auca Mahuida lavas were likely extracted from at least two mantle sources, the first one containing more garnet, thus located deep in the lithosphere (Fig. 9; green area), and the second containing more spinel, thus shallower (Fig. 9; blue area). The presence of both kinds of sources was explained by the interaction of eclogite and peridotite melts at different pressures (Søager et al., 2013; Søager and Holm, 2013), or by melting of a garnet-bearing mantle above a steepening subduction zone (Kay et al., 2013).

It has been proposed that the source of primitive basalts from Auca Mahuida volcano is characterized by a melting rate of about 4–7%, where the magmas have been in chemical equilibrium with their lherzolitic source, and finally equilibrated at the base of the lithosphere (65 to 70 km-thick; Kay et al., 2013). However, as also anticipated by Kay et al. (2013), partial melting alone could not have produced the compositional variations observed in the Auca Mahuida lava suites, and their data provide evidence for fractionation in the behavior of some incompatible elements e.g. Th (their Fig. 7a and b). Here, we have attempted to identify the relative role of the partial melting and fractional crystallization processes based on the strongly and moderately incompatible elements Th and Hf, respectively, using a Th/Hf versus Th diagram (Fig. 10). As La, Th is strongly incompatible and it is also preferentially partitioned in melt resulting from low partial melting rates. Th is therefore mainly hosted in basanitic type rocks (Fig. 8) from both high and low-MgO basalts. On the other hand, Hf, being less incompatible (and immobile) is less fractionated and it is relatively preserved during most processes such as partial melting and fractional crystallization. Fig. 10 shows that studied lavas display two trends, one involving mainly primitive and evolved basalts lying on a steep positive slope illustrating a partial melting process (Luhr et al., 1995), while fractional crystallization is evidenced by the shallower positive trend involving principally trachytic and some basaltic–andesitic rocks. Note that some basaltic–andesitic rocks lie in between both areas.

The basaltic–andesitic and trachytic rocks are characterized by a wide range of Th values (2.5–5.5 ppm and 6.5–15.5 ppm, respectively), while Th/Hf ratios remain relatively constant (between 0.8 and 1.1; Fig. 10). These features suggest that some heterogeneity is present in the mantle source, and/or that extracted magmas were stored, equilibrated and differentiated by fractional crystallization at the base of the lithosphere (Kay et al., 2013). The high Pb contents (6–20 ppm) in basaltic–andesitic and trachytic rocks suggest that a crustal contamination could have occurred during differentiation, when stored magmas interacted with the lithosphere. On the other hand, the low Pb content of primitive and evolved basalts precludes the presence of a significant crustal contamination for parent magmas (Fig. 10). Our observation agrees with previous detailed studies showing that the crustal contamination of southern PVP basalts has been shown to be very limited, with only some evidence for a small assimilation of a lower crust component by parental magmas (Kay et al., 2013; Søager et al., 2013, 2015a, 2015b). On the other hand, significant enrichment of some LILE and HFSE elements could suggest a continental lithospheric contribution for the most evolved rocks of Auca Mahuida volcano. Effectively, Figs. 5 and 10 show that K, Rb, Th, U, as well as Pb, are strongly increased in trachyandesites and trachytes, as well as in some basaltic–andesitic rocks. Such characteristics agree well with those reported in Fig. 7a and b from Kay et al. (2013), who suggest that, in Auca Mahuida, melt injection was episodic after multiple mantle melting events. In this study, we attempted to better constrain the timing of these events.

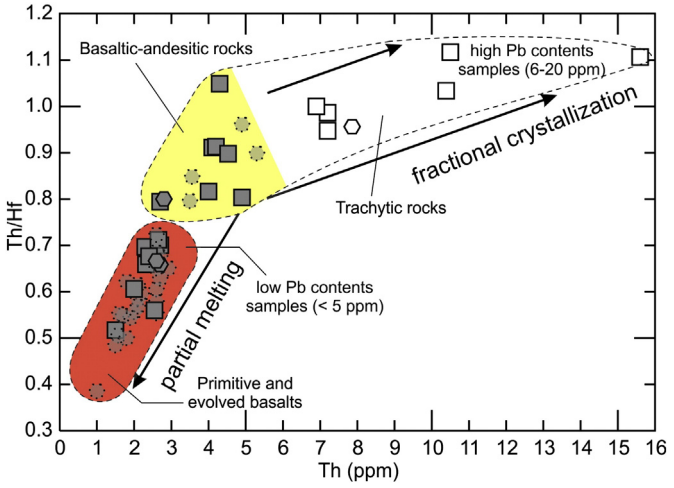

Fig. 10. Th/Hf ratio vs Th (ppm) process identification diagram of partial melting rate and fractional crystallization for Auca Mahuida lavas.

Given the good timing control available, the temporal evolution of Auca Mahuida magmas can be investigated in detail throughout the five volcanic-phases (as identified in Section 5.2). Fig. 11 shows the evolution of Mg#, Ni, some LILE (K, Pb) and HFSE (Th), from 1.8 to 1.0 Ma. For each volcanic-phase, the oldest sample (mostly a primitive basalt) has Mg# and Ni values significantly higher than the other samples. In addition, it can be observed within each phase that when Mg# and Ni decrease, the LILE and HFSE elements increase (K, Rb, Ba, Th, U, and specially Pb; Table 1 and Fig. 11). This processes appears to be cyclic between 1.78 ± 0.10 and 0.99 ± 0.04 Ma, suggesting that fractional crystallization occurred during each phase. Overall, these characteristics suggest that magmas of each volcanic-phase come from a low partial melting rate mantle source involving both garnet-bearing and spinel-bearing lherzolite sampled at different depths. There is no clear evolution of magmatic sampling from deep to shallow source within each phase. Both sources were sampled without any apparent periodicity. However, it can be observed that the first lava erupted for each phase originated from the deepest mantle source (Figs. 9 and 7). In addition, over the whole period of activity, Auca Mahuida magmas originated preferentially from the deep source during phases 1 and 2, while after phase 3, they were preferentially produced from the shallower source.

Then, the magmas extracted were stored, equilibrated and differentiated by fractional crystallization, producing basaltic–andesitic and trachytic rocks. Irrespective of the source of extraction (spinel-bearing or garnet-bearing lherzolite), we suggest that each volcanic-phase was initiated by a new batch of melt that has fed the superficial magmatic reservoirs at least five times (between 1.78 and 0.99 Ma). After the emission of primitive basalts (high-MgO) at the beginning of each phase, the fractional crystallization of basaltic magma in the lithosphere has produced the low-MgO basaltic–andesitic and trachytic rocks that were erupted at the end of each volcanic phase (Fig. 11).

5.4. Comparison with other Plio-Quaternary back-arc volcanoes

A comparison between lavas from Auca Mahuida volcano and those from the Payún area volcanoes (Payún, Payún Matrú and Los Volcanes; Germa et al., 2010; Kay et al., 2013; Søager et al., 2013; Hernando et al., 2014a, 2014b), which is the next northward large-size Quaternary volcanic complex located within the PVP, can bring strong insights regarding the spatial evolution of the magmatic source. Within K_2O vs SiO_2 diagram (Peccerillo and Taylor, 1976), Auca Mahuida volcano and Payún area volcano lavas plot along the border between high-K calc-alkaline and shoshonitic series, mainly in the basaltic and basaltic andesite fields, but also extend in the andesite field (Fig. 4a). On the contrary, SVZ arc magmas lie mainly within the calc-alkaline and

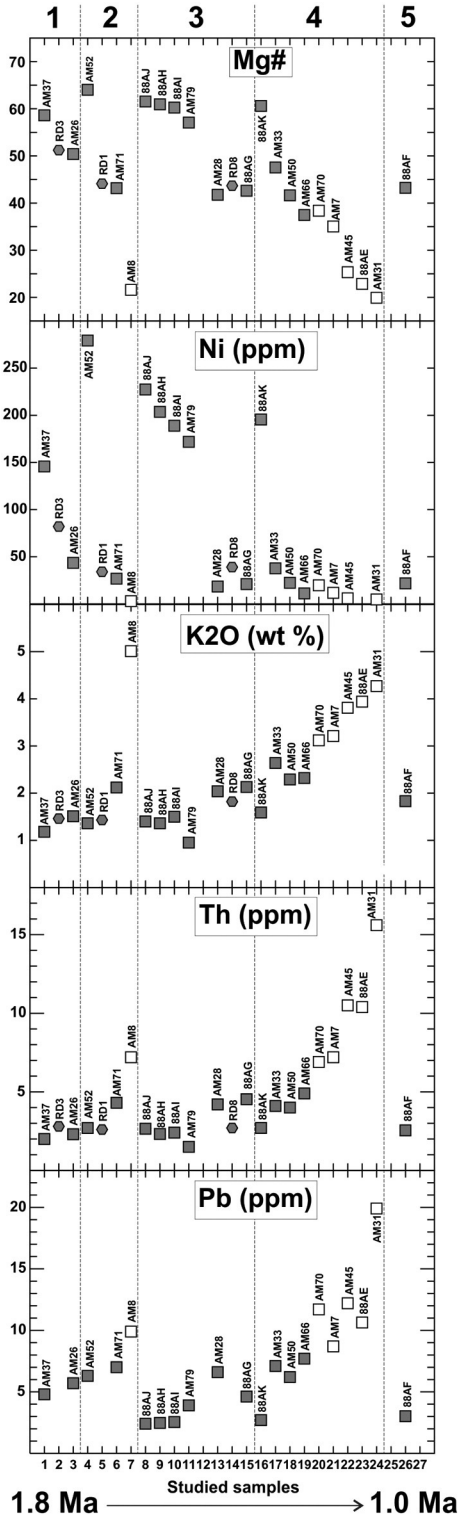

Fig. 11. Plots of Mg#, Ni, LILE (K_2O), and HFSE (Th, Pb) contents, as a function of chronologic order of studied lavas, highlighting the geochemical evolution during the five volcanic phases identified here for Auca Mahuida volcano. See text for details.

high-K calc-alkaline series. Within the TAS (total alkali silica) $Na_2O + K_2O$ vs SiO_2 diagram (Le Bas et al., 1986), Auca Mahuida volcano and Payún area volcano lavas also show strong similarities, with a slight tendency of Auca Mahuida lavas to be more alkaline (Fig. 4b).

The similarity between magmatism from these two volcanic systems can be further illustrated using the Ta/Hf ratios, which range between 0.3 and 0.6 for both of them (Fig. 12). Considering Ta/Hf values lower

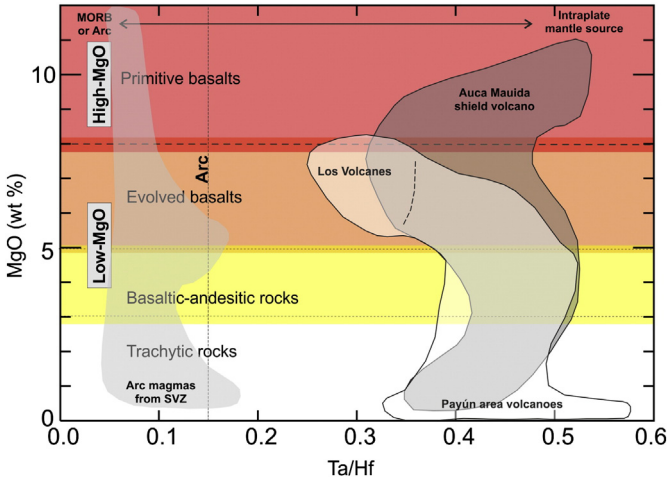

Fig. 12. MgO (wt.%) vs Ta/Hf ratio diagram for lavas from Auca Mahuida volcano, the Payún area volcanoes and arc magmas of SVZ. It also shows the main affinities (MORB-Arc and intraplate) of mantle sources.

than 0.15–0.20 as typical of lavas from the active SVZ arc (Kay et al., 2006a), both volcanic systems of Auca Mahuida volcano and the Payún area volcanoes can be associated with an intra-plate mantle source, as previously inferred (e.g., Kay et al., 2006a). However, it is worth mentioning that no primitive basalt was found in the Payún area volcanoes. Regarding the behavior of incompatible elements normalized to the primitive mantle (Sun and McDonough, 1989;

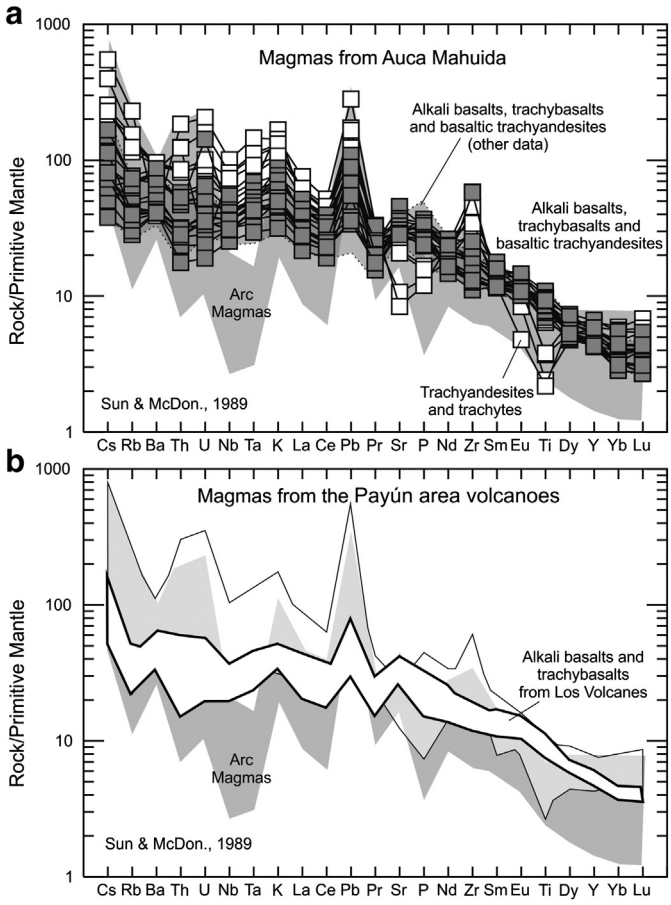

Fig. 13. Incompatible multi-element patterns of selected Plio-Quaternary lavas from Auca Mahuida volcano and the Payún area volcanoes normalized to the Primitive Mantle of Sun and McDonough (1989). Same arc magmas data as in Fig. 4.

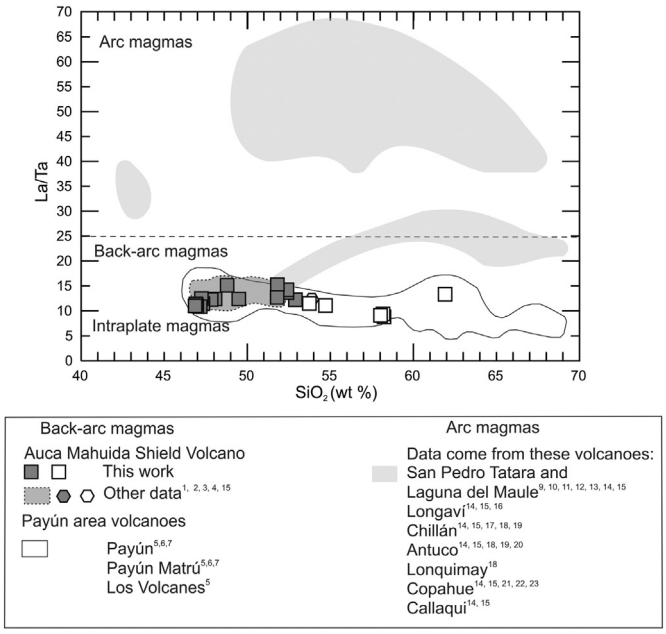

Fig. 14. La/Ta ratio vs SiO_2 (wt.%) diagram for Auca Mahuida volcano and the Payún area volcanoes lavas.
Modified from Kay et al. (2006a).

Fig. 13a and b), LILE and HFSE elements, such as Rb, U, Th, from Auca Mahuida volcano and the Payún area volcanoes are very similar. Noticeably, a sharp increase of Pb is present, although it is less pronounced for basaltic magmas from Auca Mahuida volcano and Los Volcanes (Fig. 13), which is the westernmost volcanic field of Payún area volcanoes where the less evolved basalts were erupted (Germa et al., 2010; Fig. 1). Considering Ta contents (an element not enriched in the crust), Figs. 12, 13 and 14 suggest that no significant subduction imprint is present within Auca Mahuida volcano or Los Volcanes magmas. This can be interpreted as due to a very low degree of crustal contamination for Payún area volcanoes lavas, as recently demonstrated by Sr, Nd, Hf and Pb isotopic analyses (Søager et al., 2015a). Moreover, the La/Ta ratio vs SiO_2 diagram (Fig. 14) suggests that magmas from Auca Mahuida volcano and the Payún area volcanoes (mainly Los Volcanes) have been emplaced in a back-arc context and their genesis point out to an intraplate origin (Kay et al., 2006a).

Taking into account the striking similarity between the 1.8 to 1 Ma Auca Mahuida volcano and the recent Los Volcanes magmatic field (<0. 3 Ma; Germa et al., 2010) shown here (Figs. 4, 12, 13 and 14), it can be proposed that the asthenospheric mantle source of Auca Mahuida lava has migrated northward and is probably presently in the central part of the PVP, beneath Los Volcanes magmatic field (Fig. 15). Such a hypothesis is supported by magnetotelluric data which point to the presence of shallow asthenospheric plumes underneath the Payun Matru volcano (Burd et al., 2014; Folguera et al., 2015b). In addition, note that an asthenospheric window due to slab breaking must be present to the south of Auca Mahuida (southwards of 38°S), as shown by recent seismic tomography (Pesicek et al., 2012; Folguera et al., 2015b). However, this is located south of our study area, and our data do not require this, therefore we do not show it on Fig. 15.

Finally, our data further support the hypothesis that the injection of hot asthenosphere with an OIB mantle source signature, which was triggered by the steepening of the Nazca subducting plate, induced the production of a large volume of lavas within the PVP since 2 Ma (Fig. 15; Kay, 2001; Ramos and Folguera, 2005).

6. Conclusions

The results obtained here help to further constrain the timing of the back-arc volcanic activity within the southern Payenia Volcanic Province (PVP) for the last 2 Myr.

Geochemical analyses show that Auca Mahuida magmas were extracted from at least two different OIB-type mantle sources with different depths and different garnet and spinel contents, as indicated by the La/Yb vs Yb diagram. After their extraction, magmas were stored, equilibrated and differentiated by fractional crystallization at the base of the lithosphere. Most products erupted are high-MgO basalts (primitive basalts), low-MgO basalts (evolved basalts, basaltic–andesitic rocks) and trachytic rocks.

Eleven new and four previous K–Ar ages, combined with new and previous petrographic and geochemical data show the volcanic activity of the Auca Mahuida shield volcano was rather continuous between 1.8 and 1.0 Ma. We have identified five different volcanic phases throughout the volcanic activity of Auca Mahuida volcano. The first volcanic

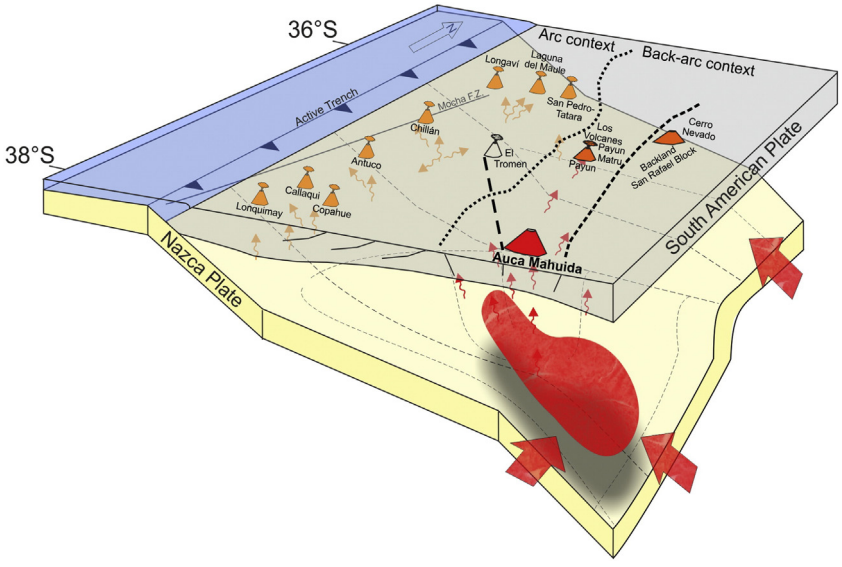

Fig. 15. Schematic model proposed for the origin of studied back-arc lavas within the Payenia Volcanic Province (PVP), showing a deformed oceanic plate and consecutive asthenospheric material upwelling. The lithospheric thickness is entirely schematic, drawn with some decrease under the PVP, according to Spagnuolo et al. (in press) and Folguera et al. (2015c).

phase is dated at around 1.78 ± 0.10 Ma (Kay et al., 2004, 2006a), but the initial activity could have been older. It is only made of evolved basalts from Pampas de las Yeguas and La Faja formations. The second phase occurred between 1.61 ± 0.02 and 1.48 ± 0.02 Ma, and it finished to build the central portion of La Faja Basalt and formed the peripheral Las Liebres Basalt and the oldest manifestation of Auca Mahuida Trachyandesite. The third volcanic-phase erupted from 1.44 ± 0.02 to 1.36 ± 0.02 Ma, and it built principally Rincon del Infiernillo together with Pampa del Leon and Cerro Grande formations. The fourth volcanic-phase erupted at 1.35 ± 0.02 Ma, ending the emplacement of the Rincon del Infiernillo formation. At 1.30 ± 0.02 Ma the Auca Mahuida group was erupted and volcanism continues at least up to 1.26 ± 0.02 Ma, when the first emission of lavas from the Puesto Retamal formation took place. Finally, the fifth and probably the youngest volcanic-phase identified, includes three stratigraphic formations: Pampa del Leon (1.18 ± 0.02 Ma), Aguada Lastra (1.17 ± 0.02 Ma) and Puesto Retamal (0.99 ± 0.04).

The decrease in Mg# and Ni contents, and increase of some incompatible elements, through time suggest that all volcanic phases (except phase 1) are characterized by an initial primitive basaltic emission (high-MgO), which evolved towards eruption of more differentiated products (low-MgO). We have observed that Auca Mahuida magmas of each volcanic-phase come from a low partial-melting rate mantle source involving both garnet-bearing and spinel-bearing lherzolite sampled at different depths. During the whole period of activity, both sources were sampled without any apparent periodicity to produce high-MgO and low-MgO basalts.

Finally, we have confirmed the striking similarity, seen by previous authors, between the petrological characteristics of the Pleistocene–Holocene basaltic rocks from Los Volcanes and those from the Auca Mahuida shield volcano. It suggests that the thermal asthenospheric anomaly, source of both magmatisms, and that was induced by slab steepening, is probably still present beneath the central part of the PVP (Fig. 15).

Acknowledgments

This work was supported by INSU-CNRS DyETI program. We thank Andrés Folguera, Victor A. Ramos and an anonymous reviewer (R#4) for their comments and suggestions that improved this manuscript. We also thank Julia Ricci and Claire Boukari for help with the K–Ar analyses. This is LGMT contribution no. 135.

References

Allègre, C.J., Treuil, M., Minster, J.F., Minster, B., Albarède, F., 1977. Systematic use of trace element in igneous processes, part I: fractional crystallization processes in volcanic suites. Contrib. Mineral. Petrol. 60, 57–75.

Ardolino, A.A., Franchi, M.R., Fauqué, L., 1995. Carta Geológica de La Provincia del Neuquén, Departamento Añelo: Buenos Aires, Programa Nacional de Cartas Geológicas de la República Argentina, Subsecretaria de Minería de la Nación, Servicio Geológico, scale 1:200,000.

Bermúdez, A., Delpino, D., Frey, F., Saal, A., 1993. Los basaltos de retroarco extraandinos. In: Ramos, V.A. (Ed.), Geología y Recursos Naturales de Mendoza, 12° Congreso Geológico Argentino and 2° Congreso de Exploración de Hidrocarburos. Relatorio. Asociación Geológica Argentina, Buenos Aires, pp. 161–172.

Bermúdez, A., Delpino, D., Zencich, S., Bolatti, N., 2000. Evolución volcanológica y petrológica del sector sur del campo volcánico Auca Mahuida, provincia del Neuquén, Argentina. 2. Actas IX Congreso Geológico Chileno, Puerto Varas, pp. 1–6.

Bertotto, G.W., Cingolani, C., Berg, E., 2009. Geochemical variations in Cenozoic back-arc basalts at the border of La Pampa and Mendoza provinces, Argentina. J. S. Am. Earth Sci. 28 (4), 360–373.

Burd, A.I., Booker, J.R., Mackie, R., Favetto, A., Pomposiello, M.C., 2014. Three-dimensional electrical conductivity in the mantle beneath the Payún Matrú Volcanic Field in the Andean backarc of Argentina near 36.5°S: evidence for decapitation of a mantle plume by resurgent upper mantle shear during slab steepening. Geophys. J. Int. 198, 812–827. http://dx.doi.org/10.1093/gji/ggu145.

Carignan, J., Hild, P., Mevelle, G., Morel, J., Yeghicheyan, D., 2001. Routine analyses of trace elements in geological samples using flow injection and low pressure online liquid chromatography coupled to ICP-MS: a study of reference materials BR, DR-N, UB-N, AN-G and GH. Geostand. Newslett. 25 (2-3), 187–198.

Cassignol, C., Gillot, P.-Y., 1982. Range and effectiveness of unspiked potassium–argon dating: experimental groundwork and applications. In: Odin, G.S. (Ed.), Numerical Dating in Stratigraphy. John Wiley & Sons, pp. 159–179 (Chptr 9).

Costa, F.G., Singer, B.S., 2002. Evolution of Holocene dacite and compositionally zoned magma, Volcan San Pedro, Southern Volcanic Zone, Chile. J. Petrol. 43, 1571–1593. http://dx.doi.org/10.1093/petrology/43.8.1571.

Deruelle, B.G., 1982. Petrology of the Plio-Quaternary volcanism of the south-central and meridional Andes. J. Volcanol. Geotherm. Res. 14, 77–124. http://dx.doi.org/10.1016/0377-0273(82)90044-0.

Deruelle, B.G., Lopez-Escobar, L., 1999. Basalts, andesites, dacites, and rhyolites from Nevados de Chilan and Antuco Stratovolcanoes (Southern Andes): a remarkable example of magmatic differentiation through crystal fractionation. C. R. Acad. Sci. Paris 2A (329), 337–344. http://dx.doi.org/10.1016/S1251-8050(00)88584-5.

Dixon, H.J., Murphy, M.D., Sparks, R.S.J., Chavez, R., Naranjo, J.A., Dunkley, P.N., Young, S.R., Gilbert, J.S., Pringle, M.R., 1999. The geology of Nevados de Chillan Volcano, Chile. Rev. Geol. Chile 26, 227–253. http://dx.doi.org/10.4067/S0716-02081999000200006.

Dungan, M.A., Wulff, A., Thompson, R., 2001. Eruptive stratigraphy of the Tatara–San Pedro complex, 36°S, Southern Volcanic Zone, Chilean Andes: reconstruction method and implications for magma evolution at long-lived arc volcanic centers. J. Petrol. 42, 555–626.

Dyhr, C.T., Holm, P.M., Llambías, E.J., Scherstén, A., 2013a. Subduction controls on Miocene back-arc lavas from Sierra de Huantraico and La Matancilla and new $^{40}Ar/^{39}Ar$ dating from the Mendoza Region, Argentina. Lithos 179, 67–83. http://dx.doi.org/10.1016/j.lithos.2013.08.007.

Dyhr, C.T., Holm, P.M., Llambías, E.J., 2013b. Geochemical constraints on the relationship between the Miocene–Pliocene volcanism and tectonics in the Palaoco and Fortunoso volcanic fields, Mendoza Region, Argentina: new insights from $^{40}Ar/^{39}Ar$ dating, Sr–Nd–Pb isotopes and trace elements. J. Volcanol. Geotherm. Res. 266, 50–68. http://dx.doi.org/10.1016/j.jvolgeores.2013.08.005.

Feeley, T.C., Dungan, M.A., Frey, F.A., 1998. Geochemical constraints on the origin of mafic and silicic magmas at Cordon El Guadal, Tatara–San Pedro Complex, Central Chile. Contrib. Mineral. Petrol. 131, 393–411. http://dx.doi.org/10.1007/s004100050400.

Fennell, L.M., Folguera, A., Naipauer, M., Gianni, G., Rojas Vera, E.A., German Bottesi, G., Ramos, V.A., 2015. Cretaceous deformation of the Southern Central Andes: synorogenic growth strata in the Neuquen Group (35°30′–37°S). Basin Res. 1–22 http://dx.doi.org/10.111/bre12135.

Ferguson, K.M., Dungan, M.A., Davidson, J.P., Colucci, M.T., 1992. The Tatara–San Pedro Volcano, 36°S, Chile: a chemically variable, dominantly mafic magmatism system. J. Petrol. 33, 1–43.

Folguera, A., Naranjo, J.A., Orihashi, Y., Sumino, H., Nagao, K., Polanco, E., Ramos, V.A., 2009. Retroarc volcanism in the northern San Rafael block (34°–35°30′S), Southern Central Andes: occurrence, age, and tectonic setting. J. Volcanol. Geotherm. Res. 186, 169–185.

Folguera, A., Alasonati Tašárová, Z., Götze, H.J., Rojas Vera, E., Giménez, M., Ramos, V.A., 2015a. Retroarc extension in the last 6 Ma in the South-Central Andes (36°Se40°S) evaluated through a 3-D gravity modelling. J. S. Am. Earth Sci. 40, 23–37. http://dx.doi.org/10.1016/j.jsames.2012.08.003.

Folguera, A., Bottesi, G., Duddy, I., Martín-González, F., Orts, D., Sagripanti, L., Rojas Vera, E., Ramos, V.A., 2015b. Exhumation of the Neuquén Basin in the Southern Central Andes (Malargüe fold and thrust belt) from field data and low-temperature thermochronology. J. S. Am. Earth Sci. 64, 381–398.

Folguera, A., Gianni, G., Sagripanti, L., Rojas Vera, E., Novara, I., Colavitto, B., Alvarez, O., Orts, D., Tobal, J., Giménez, M., Introcaso, A., Ruiz, F., Martínez, P., Ramos, V.A., 2015c. A review about the mechanisms associated with active deformation, regional uplift and subsidence in southern South America. J. S. Am. Earth Sci. 64, 511–529.

Frey, F.A., Gerlach, D.C., Hickey, R.L., Lopez-Escobar, L., Munizaga-Villavicencio, F., 1984. Petrogenesis of the Laguna del Maule Volcanic Complex, Chile (36° S). Contrib. Mineral. Petrol. 88 (1-2), 133–149.

Fuhrmann, U., Lippolt, H.J., Hess, J.C., 1987. Examination of some proposed K–Ar standards — $^{40}Ar/^{39}Ar$ analyses and conventional K–Ar data. Chem. Geol. 66 (1-2), 41–51.

Germa, A., Quidelleur, X., Gillot, P.-Y., Tchilinguirian, P., 2010. Volcanic evolution of the back-arc Pleistocene Payún Matrú volcanic field (Argentina). J. S. Am. Earth Sci. 29, 717–730.

Germa, A., Quidelleur, X., Lahitte, P., Labanieh, S., Chauvel, C., 2011. The K–Ar Cassignol–Gillot technique applied to western Martinique lavas: a record of the evolution of the recent Lesser Antilles island arc activity from 2 Ma to Mount Pelée volcanism. Quat. Geochronol. 6, 341–355.

Gillot, P.-Y., Cornette, Y., 1986. The Cassignol technique for potassium-argon dating, precision and accuracy: examples from late Pleistocene to recent volcanics from southern Italy. Chem. Geol. 59, 205–222.

Gillot, P.-Y., Cornette, Y., Max, N., Floris, B., 1992. Two reference materials, trachytes MDO-G and ISH-G, for argon dating (K–Ar and $^{40}Ar/^{39}Ar$) of Pleistocene and Holocene rocks. Geostand. Newslett. 16 (1), 55–60.

Gillot, P.-Y., Hildenbrand, A., Lefèvre, J.-C., Albore-Livadie, C., 2006. The K/Ar dating method: principle, analytical techniques, and application to Holocene volcanic eruptions in southern Italy. Acta Vulcanol. 18 (2), 55–66.

Govindaraju, K., Mevelle, G., 1987. Fully automated dissolution and separation methods for inductively coupled plasma atomic emission spectrometry rock analysis. Application to the determination of rare earth elements. J. Anal. At. Spectrom. 2, 615–621.

Govindaraju, K., Potts, P.J., 1994. 1994 report on Whin sill doleroite WS–E from England and Pitscurrie microgabbro PM-S from Scotland: assessment by one hundred and four international laboratories. Geostand. Newslett. 18 (2), 211–300.

Gudnason, J., Holm, P.M., Søager, N., Llambías, E.J., 2012. Geochronology of the late Pliocene to recent volcanic activity in the Payenia back-arc volcanic province, Mendoza Argentina. J. S. Am. Earth Sci. 37, 191–201.

Hernando, I.R., Llambías, E.J., González, P.D., Sato, K., 2012. Volcanic stratigraphy and evidence of magma mixing in the Quaternary Payún Matrú volcano, Andean backarc in western Argentina. Andean Geol. 39 (1), 158–179.
Hernando, I.R., Aragón, E., Frei, R., González, P.D., Spakman, W., 2014a. Constraints on the origin and evolution of magmas in the Payún Matrú Volcanic Field, Quaternary Andean Back-arc of western Argentina. J. Petrol. 55 (1), 209–239. http://dx.doi.org/10.1093/petrology/egt066.
Hernando, I.R., Franzese, J.R., Llambías, E.J., Petrinovic, I.A., 2014b. Vent distribution in the Quaternary Payún Matrú Volcanic Field, western Argentina: its relation to tectonics and crustal structures. Tectonophysics 622, 122–134. http://dx.doi.org/10.1016/j.tecto.2014.03.003.
Hess, J.C., Lippolt, H.J., 1994. Compilation of K–Ar measurements on HD-B1 standard biotite: 1994 status report. In: Odin, G.S. (Ed.), Calibration of the Phanerozoic Time Scale, IGCP Proj. 196. IUGS Subcomm. on Geochronol. International Geological Correlation Programme, Paris, pp. 19–23.
Holmberg, E., 1964. Descripción geológica de la Hoja 33d, Auca Mahuida (Provincia del Neuquén). Dirección Nacional de Geología y Minería. Buenos Aires. Boletín 94, 1–88.
Irvine, T.N., Baragar, W.R.A., 1971. A guide to the chemical classification of the common rocks. Can. J. Earth Sci. 8, 523–548.
Jacques, G., Hoernle, K., Gill, J., Hauff, F., Wehrmann, H., Garbe-Schönberg, D., van den Bogaard, P., Bindeman, I., Lara, L.E., 2013. Across-arc geochemical variations in the Southern Volcanic Zone, Chile (34.5–38.0°S): constraints on mantle wedge and slab input compositions. Geochim. Cosmochim. Acta 123, 218–243.
Kay, S., 2001. Tertiary to recent magmatism and tectonics of the Neuquén basin between 36°05′ and 38°S latitude. Buenos Aires, Internal report to Repsol YPF (125 pp.).
Kay, S.M., Gorring, M., Ramos, V.A., 2004. Magmatic sources, setting and causes of Eocene to Recent Patagonian plateau magmatism (36° to 52°S latitude). Rev. Asoc. Geol. Argent. 59 (4), 556–568 (ISSN 0004-4822).
Kay, S.M., Burns, M., Copeland, P., Mancilla, O., 2006a. Upper Cretaceous to Holocene magmatism and evidence for transient Miocene shallowing of the Andean subduction zone under the northern Neuquén Basin. In: Kay, S.M., Ramos, V.A. (Eds.), Evolution of an Andean Margin: A Tectonic and Magmatic View From the Andes to the Neuquén Basin (35–39°S). Geological Society of America, Special Paper 407, pp. 19–60.
Kay, S.M., Mancilla, O., Copeland, P., 2006b. Evolution of the backarc Chachahuén volcanic complex at 37°S latitude over a transient Miocene shallow subduction zone under the Neuquén Basin. In: Kay, S.M., Ramos, V.A. (Eds.), Evolution of an Andean Margin: A Tectonic and Magmatic View From the Andes to the Neuquén Basin (35–39°S). Geological Society of America, Special Paper 407, pp. 215–246.
Kay, S.M., Jones, H.A., Kay, R.W., 2013. Origin of Tertiary to Recent EM – and subduction – like chemical and isotopic signatures in Auca Mahuida region (37°–38°S) and other Patagonian plateau lavas. Contrib. Mineral. Petrol. 166, 165–192. http://dx.doi.org/10.1007/s00410-013-0870-9.
Kuiper, K.F., Deino, A., Hilgen, F.J., Krijgsman, W., Renne, P.R., Wijbrans, J.R., 2008. Synchronizing rock clocks of earth history. Science 320, 500–504.
Le Bas, M.J., Le Maitre, R.W., Streckeisen, A., Zanettin, B., 1986. A chemical classification of volcanic rocks based on the total alkali-silica diagram. J. Petrol. 27, 745–750.
Litvak, V.D., Spagnuolo, M.G., Folguera, A., Poma, S., Jones, R.E., Ramos, V.A., 2015. Late Cenozoic calc-alkaline volcanism over the Payenia shallow subduction zone, South Central Andean back-arc (34°30′–37°S), Argentina. J. S. Am. Earth Sci. 64, 365–380. http://dx.doi.org/10.1016/j.jsames.2015.09.010.
Llambías, E.J., Bertotto, G.B., Risso, C., Hernando, I., 2010. El volcanismo Cuaternario en el retroarco Payenia: una revisión. Rev. Asoc. Geol. Argent. 67-2, 278–300.
Lopez-Escobar, L., Vergara, M.M., Frey, F.A., 1981. Petrology and geochemistry of lavas from Antuco Volcano, a basaltic volcano of the Southern Andes (37°25′). J. Volcanol. Geotherm. Res. 11, 329–352. http://dx.doi.org/10.1016/0377-0273(81)90030-5.
Luhr, J.F., Aranda-Gómez, J.J., Housh, T.B., 1995. San Quintin Volcanic field, Baja California Norte, México. Geology, petrology, and geochemistry. J. Geophys. Res. 100, 10,353–10,380.
Macdonald, G.A., Katsura, T., 1964. Chemical composition of Hawaiian lavas. J. Petrol. 5, 82–133.
Muñoz, J.B., Stern, C.R., 1988. The Quaternary volcanic belt of the southern continental margin of South America: traverse structural and petrochemical variations across the segment between 38°S and 39°S. J. S. Am. Earth Sci. 1, 147–161. http://dx.doi.org/10.1016/0895-9811(88)90032-6.
Muñoz, J.B., Stern, C.R., Bermudez, A., Delpino, D., Dobbs, M.F., Frey, F.A., 1989. Plio-Quaternary volcanism between 34–39°S of the Andes. Rev. Asoc. Geol. Argent. 44, 270–286.
Peccerillo, A., Taylor, S.R., 1976. Geochemistry of Eocene calcalkaline volcanic rocks from the Kastamonu area, northern Turkey. Contrib. Mineral. Petrol. 58, 63–81.
Pesicek, J.D., Engdahl, E.R., Thurber, C.H., DeShon, H.R., Lange, D., 2012. Mantle subducting slab structure in the region of the 2010 M8.8 Maule earthquake (30–40°S), Chile. Geophys. J. Int. 191, 317–324. http://dx.doi.org/10.1111/j.1365-246X.2012.05624.x.
Pichavant, M., Mysen, B.O., Macdonald, R., 2002. Source and H_2O content of high-MgO magmas in island arc settings: an experimental study of a primitive calc-alkaline basalt from St. Vincent, Lesser Antilles arc. Geochim. Cosmochim. Acta 66 (12), 2193–2209.
Quidelleur, X., Gillot, P.-Y., Soler, V., Lefèvre, J.C., 2001. K/Ar dating extended into the last millennium: application to the youngest effusive episode of the Teide Volcano (Spain). Geophys. Res. Lett. 28 (16), 3067–3070.
Quidelleur, X., Carlut, J., Tchilinguirian, P., Germa, A., Gillot, P.-Y., 2009. Paleomagnetic directions from mid-latitude sites in the southern hemisphere (Argentina): contribution to time averaged field models. Phys. Earth Planet. Inter. 172, 199–209.
Ramos, V.A., Folguera, A., 2005. Tectonic evolution of the Andes of Neuquén: constraints derived from the magmatic arc and foreland deformation. In: Veiga, G., et al. (Eds.), The Neuquén Basin: A Case Study in Sequence Stratigraphy and Basin Dynamics. The Geological Society, Special Publication 252, pp. 15–35.
Ramos, V.A., Folguera, A., 2011. Payenia volcanic province in the Southern Andes: an appraisal of an exceptional Quaternary tectonic setting. J. Volcanol. Geotherm. Res. 201, 53–64.
Ramos, V.A., Kay, S., 2006. Overview of the tectonic evolution of the Southern Central Andes of Mendoza and Neuquen (35°–39°S). In: Kay, S.M., Ramos, V.A. (Eds.), Evolution of an Andean Margin: A Tectonic and Magmatic View From the Andes to the Neuquén Basin (35°–39°S Lat). Geological Society of America, Special Paper 407, pp. 1–17.
Ramos, V.A., Litvak, V.D., Folguera, A., Spagnuolo, M., 2014. An Andean tectonic cycle: from crustal thickening to extension in a thin crust (34°–37°SL). Geosci. Front. 5, 351–367.
Rodríguez, C., Sellés, D., Dungan, M., Langmuir, C., Leeman, W., 2007. Adakitic dacites formed by intracrustal crystal fractionation of water-rich parent magmas at Nevado de Longaví Volcano (3628S; Andean SouthernVolcanic Zone, Central Chile). J. Petrol. 48 (11), 2033–2061. http://dx.doi.org/10.1093/petrology/egm049.
Rossello, E.A., Cobbold, P.R., Diraison, M., Arnaud, N., 2002. Auca Mahuida (Neuquén Basin, Argentina): a Quaternary shield volcano on a hydrocarbon-producing substrate. 5° International Symposium on Andean Geodynamics, Extended Abstracts, pp. 549–552 (Toulouse).
Samper, A., Quidelleur, X., Boudon, G., Le Friant, A., Komorowski, J.C., 2008. Radiometric dating of three large volume flank collapses in the Lesser Antilles arc. J. Volcanol. Geotherm. Res. 176, 485–492.
Schwarz, W.H., Trieloff, M., 2007. Intercalibration of Ar-40–Ar-39 age standards NL-25, HB3gr hornblende, GA1550, SB-3, HD-B1 biotite and BMus/2 muscovite. Chem. Geol. 242 (1-2), 218–231.
Søager, N., Holm, P.M., 2013. Melt-peridotite reactions in upwelling eclogite bodies: constraints from EM1-type alkaline basalts in Payenia, Argentina. Chem. Geol. 360-361, 204–219. http://dx.doi.org/10.1016/j.chemgeo.2013.10.024.
Søager, N., Holm, P.M., Llambías, E.J., 2013. Payenia volcanic province, southern Mendoza, Argentina: OIB mantle upwelling in a backarc environment. Chem. Geol. 349-350, 36–53. http://dx.doi.org/10.1016/j.chemgeo.2013.04.007.
Søager, N., Holm, P.M., Thirlwall, M.F., 2015a. Sr, Nd, Pb and Hf isotopic constraints on mantle sources and crustal contaminants in the Payenia volcanic province, Argentina. Lithos 212-215, 368–378.
Søager, N., Portnyagin, M., Hoernle, K., Holm, P.M., Hauff, F., Garbe-Schönberg, D., 2015b. Olivine major and trace element compositions in Southern Payenia Basalts, Argentina: evidence for pyroxenite–peridotite melt mixing in a back-arc setting. J. Petrol. 2015, 1–24. http://dx.doi.org/10.1093/petrology/egv043.
Spagnuolo, M.G., Orts, D.L., Gimenez, M., Folguera, A., Ramos, V.A., 2015. Payenia Quaternary flood basalts (southern Mendoza, Argentina): geophysical constraints on their volume. Geosci. Front. 1–8 http://dx.doi.org/10.1016/j.gsf.2015.10.004 (in press).
Steiger, R.H., Jäger, E., 1977. Subcommission on geochronology: convention on the use of decay constants in geo and cosmochronology. Earth Planet. Sci. Lett. 36 (3), 359–362.
Stern, C.R., 2004. Active Andean volcanism: its geologic and tectonic setting. Rev. Geol. Chile 31-2, 161–206.
Sun, S.S., McDonough, W.F., 1989. Chemical and isotopic systematics of oceanic basalts: implications for mantle composition and processes. In: Saunders, A.D., Norry, M.J. (Eds.), Magmatism in the Ocean Basin. Geological Society of London Special Publication vol. 42, pp. 313–345.
Thompson, R.N., 1984. Dispatches from the basalt front; I, experiments. Proc. Geol. Assoc. 95 (3), 249–262.
Varekamp, J.C., Maarten deMoor, J., Merrill, M.D., Colvin, A.S., Goss, A.R., Vroon, P.Z., Hilton, D.R., 2006. Geochemistry and isotopic characteristics of the Caviahue–Copahue volcanic complex, Province of Neuquén, Argentina. In: Kay, S.M., Ramos, V.A. (Eds.), Evolution of an Andean Margin: A Tectonic and Magmatic View From the Andes to the Neuquén Basin (35–39°S). Geological Society of America, Special Paper 407, pp. 317–342. http://dx.doi.org/10.1130/2006.2407(15).
Ventura, G., De Ritis, R., Longo, M., Chiappini, M., 2012. Terrain characterization and structural control of the Auca Mahuida volcanism (Neuquén Basin, Argentina). Int. J. Geogr. Inf. Sci. 1–12 http://dx.doi.org/10.1080/13658816.2012.741241.
Villemant, B., Jaffrezic, H., Joron, J.L., Treuil, M., 1981. Distribution coefficients of major and trace elements: fractional crystallization in the alkali basalts series of Chaine des Puys (Massif Central, France). Geochim. Cosmochim. Acta 45, 1997–2016.
Yoder, H.S., Tilley, C.E., 1962. Origin of basalt magmas: an experimental study of natural and synthetic rock systems. J. Petrol. 3, 342–532.